

Increasing Fe Tolerance of 6022 Aluminum Sheet for Hemming Applications

by

Alexis Leigh Pleva

Chemistry, BS Seton Hill University, 2001
MBA, Seton Hill University, 2003

Submitted to the Graduate Faculty of the
Swanson School of Engineering in partial fulfillment
of the requirements for the degree of
Master of Science

University of Pittsburgh

2023

UNIVERSITY OF PITTSBURGH

SWANSON SCHOOL OF ENGINEERING

This thesis was presented

by

Alexis Leigh Pleva

It was defended on

July 17, 2023

and approved by

Prof. Markus Chmielus, PhD, Mechanical Engineering & Materials Science Department

Prof. Jung-Kun Lee, PhD, Mechanical Engineering & Materials Science Department

Thesis Advisor: Prof. Zachary Harris, PhD, Mechanical Engineering & Materials Science
Department

Copyright © by [Alexis Leigh Pleva]

2023

Increasing Fe Tolerance of 6022 Aluminum Sheet for Hemming Applications

Alexis Leigh Pleva

University of Pittsburgh, 2023

Increasing awareness of the impact that industrial processes have on the environment has broadly motivated efforts to better balance economic and environmental sustainability. The automotive industry is increasingly interested in leveraging scrap-based aluminum alloys due to (1) the lightweighting benefits of aluminum relative to steel components and (2) the 95% reduction in energy costs associated with fabricating scrap-based versus prime-based aluminum alloys. However, the adoption of scrap-based aluminum alloys is complicated by the expected increase in trace impurities, such as Fe, which are known to affect the mechanical behavior and formability of aluminum alloy sheet. As such, it is critical that strategies be developed to increase the tolerance of automotive aluminum sheet alloys to increasing impurity content.

In this thesis, the effect of modifications to the bulk alloy composition (Si-to-Mg ratio) and extent of cold work on the microstructure, mechanical properties, and formability of AA6022 containing either high or low Fe content is studied. Results reveal that modifications in bulk alloy composition do affect the mechanical behavior and formability, but does not significantly improve the Fe tolerance. Conversely, increasing the cold work level broadly resulted in acceptable levels of formability for both evaluated Fe contents. This behavior is linked to the propensity of the higher cold work level to promote more homogeneous grain structure and a smaller grain size, which are known to promote good formability. The thesis concludes with initial correlations between hem performance and obtained mechanical properties to help guide future material selection efforts.

Table of Contents

1.0 Introduction.....	1
1.1 Background.....	1
1.2 Overarching Objectives and Governing Hypotheses	7
1.3 Organization of Thesis	8
2.0 Methods.....	9
2.1 Materials.....	9
2.2 Processing.....	10
2.3 Microstructural Characterization	12
2.3.1 Metallographic Preparation.....	13
2.3.2 Optical Microscopy and Analysis	14
2.3.3 Electron Microscopy and Analysis	14
2.4 Mechanical Property Evaluations.....	16
2.4.1 Uniaxial Tensile Testing	16
2.4.2 Formability Testing.....	17
3.0 Results	22
3.1 Microstructure Evaluation	22
3.1.1 Secondary Phase Particles	22
3.1.2 Grain Structure	25
3.2 Mechanical Testing Results	29
3.3 Formability.....	37
3.3.1 Flat Hemming.....	39

4.0 Discussion.....	42
4.1 Role of Cold Work and Minor Primary Element Modifications for Creating Fe-Tolerant Automotive Al Sheet Alloys	43
4.2 Correlation of Bulk Mechanical Properties with Hemming Performance	46
5.0 Conclusions.....	50
6.0 Recommendation and Future Work	52
Bibliography	54

List of Tables

Table 1: Al vs. Steel Savings on Commercial Vehicles	1
Table 2: Overview of tested alloys' characteristics.....	10
Table 3: AA6022 Chemical Composition.....	10
Table 4: Metallographic sample preparation procedure	13
Table 5: Grain Size Measurements	26
Table 6: Summary of microstructural and mechanical (after 180 d of natural aging) metrics for each alloy condition; note that TYS is in MPa, VDA is in degrees, and GS is in μm.....	42

List of Figures

Figure 1: Schematic overview of the primary aluminum production process [13]	3
Figure 2: Distribution of U.S. aluminum production between primary and secondary aluminum since 1980.....	4
Figure 3: Schematic (top) and cross-section (bottom) of a typical flat hem.....	5
Figure 4: Overview schematic of typical thermomechanical processing steps for automotive Al sheet.....	11
Figure 5: Schematic of typical grain structure evolution during thermomechanical processing of Al sheet alloys.....	12
Figure 6: Typical optical image of the microstructure; original magnification was 200X ..	14
Figure 7: SEM images before and after segmentation.	15
Figure 8: Typical stress-strain curve for AA6022-T4, with work hardening regime indicated.	17
Figure 9: Schematic of the (left) VDA setup and (right) bend angle [52]	19
Figure 10: Flat hem testing schematic [55].....	20
Figure 11: Typical ranking criteria used to evaluate hems	21
Figure 12: SEM backscatter electron images of each alloy microstructure after solution heat treat	23
Figure 13: EDS of (middle) bright particles and (bottom) matrix region of the SEM micrograph (top)	24
Figure 14: EBSD IPF maps of the eight evaluated materials	25
Figure 15: Effect of f/r on the average grain size for each tested alloy condition.....	27

Figure 16: Variation in fraction of grains with cube texture for each condition. The number above each bar indicates the average grain size for that respective alloy condition (in micrometers) and the error bars correspond to the standard deviation of multiple measurements..... 28

Figure 17: Tensile yield strength as a function of natural aging time. The lines correspond to OEM-mandated maximum values at 30, 90, and 180 d..... 30

Figure 18: Yield strength after 30, 90, and 180 d of natural aging for each alloy 31

Figure 19 Effect of natural aging kinetics on the strain hardening exponent (from 10-20% strain) for each tested alloy condition. 32

Figure 20: Variation in n-value (10-20%) as a function of loading direction after 180 d of natural aging..... 33

Figure 21: Measured r-value at 10% elongation for each alloy condition parallel to the L direction as a function of natural aging time..... 34

Figure 22: Measured r_m for each tested condition after 180 d of natural aging. 35

Figure 23: Measured r-value along the L, LT, and 45 directions for each alloy condition after 10% elongation and 180 d of natural aging..... 36

Figure 24: Measured bend angles via VDA testing for each alloy condition after 30, 90, and 180 d of natural aging. Note that error bars correspond to the standard deviation of multiple measurements..... 38

Figure 25: Images of the flat hem samples after 180 d of natural aging..... 39

Figure 26: Hem ratings (L direction oriented parallel to the bend line) as a function of natural aging time for each tested alloy condition..... 40

Figure 27: Images of A2_65CW_LF flat hems after 30, 90, and 180 d of natural aging..... 41

Figure 28: Effect of f/r on hem rating after 180 d of natural aging for each alloy condition.
..... 45

Figure 29: Effect of grain size on the hem rating of each condition after 180 d of natural aging. 46

Figure 30: Comparison of mechanical testing metrics and measured hem ratings at 180 d of natural aging...... 48

1.0 Introduction

1.1 Background

Increasing awareness of the impact that industrial processes have on the environment has broadly motivated efforts to better balance economic and environmental sustainability. For example, government regulations [1] and increasing consumer interest [2] have motivated efforts to increase the fuel efficiency of passenger vehicles. One avenue for improving a vehicle's fuel economy is through the replacement of high-weight components with less-dense materials (i.e., lightweighting) [3–5]. The weight savings of such a material change can be significant, often reaching 50% for an individual component as documented in the analysis performed by Wang [6], reported in Table 1. Towards this end, Ford replaced numerous steel body and closure components in the F-150 truck with aluminum alloys in 2015, resulting in a decrease of ~320 kg in curb weight and a nominal 20% improvement in fuel efficiency [7].

Table 1: Al vs. Steel Savings on Commercial Vehicles

Application	Steel (kg)	Aluminum (kg)	Typical Wt. Savings (kg)	% Saving
Hood	16	8	8	50
Fenders	7	3.5	3.5	50
Deck lid	17	9	8	47
Doors	73	43	30	41
BIW Doors	328	209	119	36
Total	441	272.5	168.5	45

This material change, along with Department of Energy-funded concept design efforts like the Multi-Material Lightweight Vehicle (MMLV) [4], demonstrated that lightweighting and the concomitant increase in fuel efficiency can be accomplished without significant increases in a vehicle's price [7]. This has led to expanded use of aluminum alloys in other vehicle platforms [8], with Al alloys now employed for door outers and inners, struts, hoods, and even safety-critical, body-in-white components [3,8,9]. However, this increase in fuel efficiency via the use of aluminum alloys comes at a cost as aluminum is one of the most energy-intensive structural metals to produce, requiring up to 7-fold more energy per kg than steel [10].

The high energy cost of creating prime aluminum from bauxite ore is driven by the expensive nature of multiple steps throughout the production process, which is schematically shown in Figure 1 [11]. For example, after the ore is extracted, it must undergo the Bayer process to convert the bauxite to alumina. This involves multiple digestion steps, necessitating both high energy inputs but also the generation of toxic byproducts like caustic mud that must be properly disposed of to avoid contamination of water sources [12]. Once the alumina is produced, it is then reduced to form aluminum via the Hall-Heroult process, which involves the passage of large currents (~250,000 A) at high temperature (950 °C) using carbon anodes suspended in cryolite (sodium aluminum fluoride salt). Not only is this process inherently energy-intensive (~14 kW/kg), but also results in the generation of polluting byproducts that must be managed [12]. Moreover, the large power demand also inherently leads to secondary pollution through the power generation process, leading to the emission of carbon dioxide and other greenhouses that contribute to global warming.

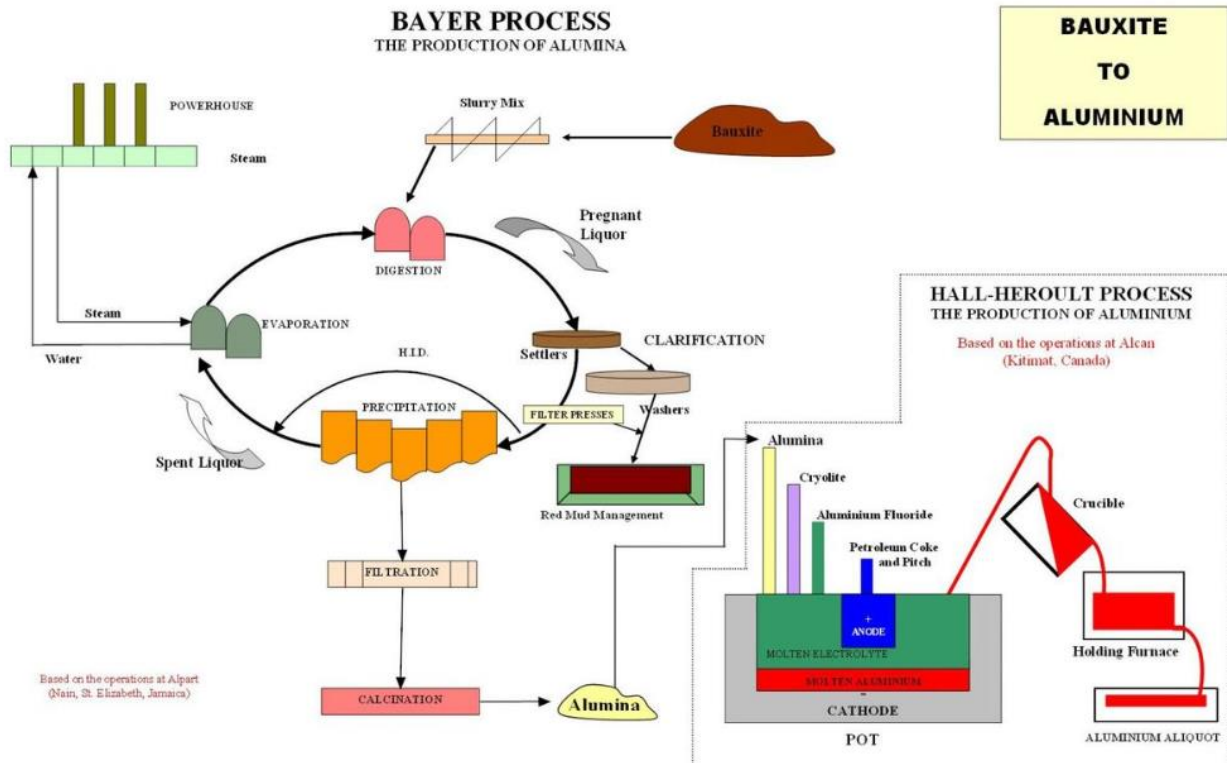


Figure 1: Schematic overview of the primary aluminum production process [13] Reprinted from Elsevier Books, A. T. Tabereaux, Treatise on Process Metallurgy, Copyright (2014), with permission from Elsevier

While manufacturing prime aluminum alloys from bauxite ore is energy-intensive, analysis has shown that creating the same alloy from remelting of aluminum scrap uses only 5% of the energy required for prime-based production [14]. In fact, industry data [15] demonstrates that scrap-based alloys (though much of this scrap is ‘high-quality’; generated during production rather than recovered from the field) are already a significant fraction of U.S. based production, as shown in Figure 2. This reduced energy cost, coupled with the large projected increase in available scrap aluminum due to the recycling of vehicles [8], has motivated interest in fabricating automotive aluminum alloys from vehicle scrap [10,16-18]. However, the effective implementation of this circular economy is hindered by two key materials-related challenges [10]. First, multiple types of aluminum alloys are currently employed across a typical automotive platform, with most being Al-Mg-Si (6xxx-series), Al-Mg (5xxx-series), and high Si-containing cast (A300-series) alloys

[16,19]. As such, there could be inherent variability in scrap composition that is difficult to predict or control [9]. For example, the accidental inclusion of cast aluminum alloys (high Si), 2xxx-series alloys (high Cu), 7xxx-series alloys (high Zn), or even an overabundance of 5xxx-series alloys (high Mg), in the scrap stream would result in a recycled alloy that does not meet current compositional specifications [16,18]. Moreover, given that the performance of automotive aluminum alloys is sensitive to minor changes in bulk elements [20-30], such inconsistencies could compromise performance and become a roadblock to the broader implementation of scrap-based alloys.

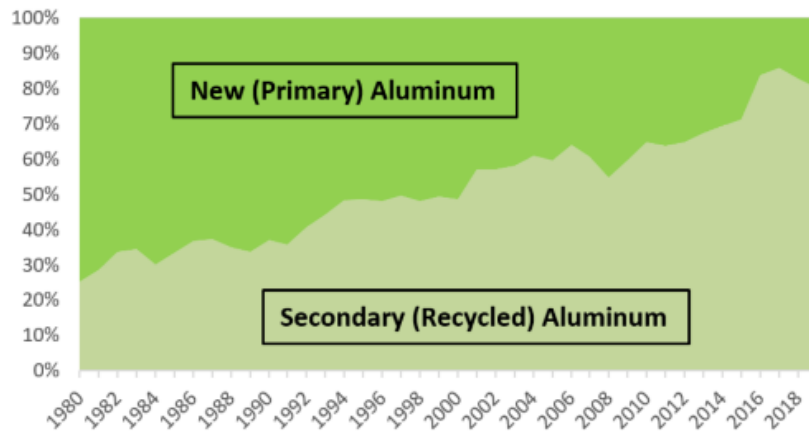


Figure 2: Distribution of U.S. aluminum production between primary and secondary aluminum since 1980.

Second, in addition to these concerns about the variation in primary alloying elements (Mg, Si, Mn, Cu, etc.), it is expected that trace elements will accumulate during alloy recycling. For example, literature suggests that V may increase with recycling [31], which could affect natural aging kinetics in 6xxx-series alloys (though reports differ on impact [32–34]), modify recrystallization behavior [31], and contribute to the formation of insoluble intermetallic particles [36]. Similar concerns have been raised regarding trace Zr, Ni, and Cr [31]. However, the primary trace element of concern is Fe, which is expected to significantly increase in recycled aluminum alloys due to interactions with shredding equipment and steel contamination in the scrap recycling

stream [10]. While increased Fe can be beneficial by refining the size of constituent particles and improving recrystallization kinetics, it is known to reduce the ductility of 6xxx-series Al sheet alloys, likely leading to reduced formability [10,35]. However, despite this expected accumulation, specific studies of Fe content influences relevant to performance of 6xxx-series automotive alloys are generally limited in the open literature, with most studies using unrealistic Fe contents (>1 wt. %) [37] or non-relevant processing (such as high-pressure torsion) [38].

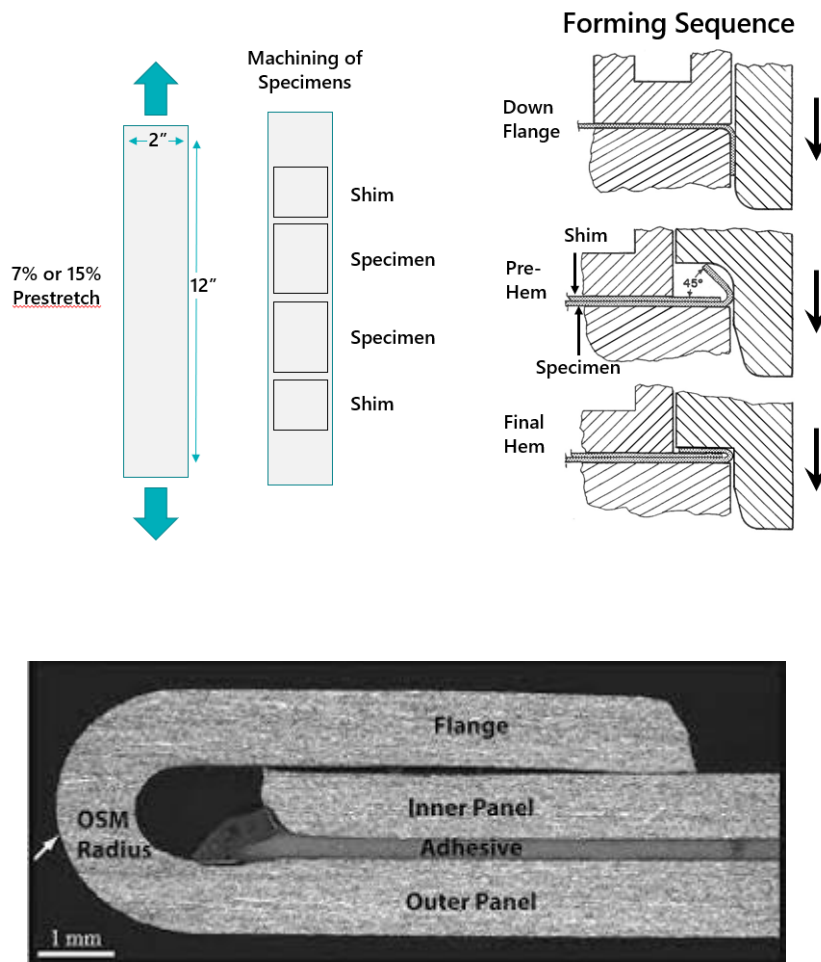


Figure 3: Schematic (top) and cross-section (bottom) of a typical flat hem.

Of particular concern is the effect of these trace elements induced by recycling on the formability of automotive sheet alloys, which often undergo complex and demanding forming operations to achieve desired shapes. For example, hemming is a process that joins separate sheets through bending/folding to form panels that are commonly used in the automotive industry for hoods, doors and tailgates [39]. A schematic of the hemming process and cross-section of a typical hem are shown in Figure 3. Hemming is performed to provide a better geometry for the vehicle, add rigidity to the structure, and to allow for safe handling of the part. However, because of the degree of deformation needed to create hems, highly formable alloys are needed that can also meet specific strength targets mandated by original equipment manufacturers (OEMs) [40]. Increasing Fe content would be expected to reduce alloy formability due to the increase in Fe-rich constituent particles and subsequent deleterious effect on ductility. Yet, despite this potential negative impact, dedicated studies looking at the effect of trace elements on hemming performance are not available in the open literature.

To broaden the adoption of scrap-based aluminum alloys in the automotive industry, it is clear these compositional-based challenges must be overcome. The most common proposed mitigation strategy is to improve the quality of the aluminum scrap stream through the implementation of more robust sorting [10,16,19]. However, this approach is hindered for two reasons: (1) the distributed nature of scraping operations makes this logistically intractable to rigorously manage and (2) the proliferation of ‘similar, but different’ aluminum alloys that are used for the same component. For example, AA6005, AA6009, AA6010, AA6014, AA6016, AA6022, AA6111, and AA6451 are all currently registered for use in automotive outer panels [9] and are challenging to differentiate given their similar (but importantly different) compositions.

Recognition of these challenges has motivated a second oft-proposed approach, which involves the intentional development of new alloys based on the expected composition of incoming aluminum scrap streams [3,10,19]. However, as discussed above, there is considerable uncertainty in the composition of aluminum scrap, which could complicate efforts to design and register new alloys for use in automotive applications. Given these barriers, a third approach has been proposed, which involves modification of current alloy compositions or thermomechanical processing approaches to create more ‘scrap-tolerant’ alloys that maintain performance in the face of expected impurities. However, in order for this approach to be implemented, significant increases in the understanding of how trace elements impact processing-property-structure relationships in automotive aluminum alloys must be achieved.

1.2 Overarching Objectives and Governing Hypotheses

The preceding background establishes that recycling-tolerant aluminum sheet alloys for automotive applications must meet required performance specifications despite the presence of increased deleterious impurities. However, the necessary understanding required to targetedly modify existing alloys to increase their tolerance of accumulated impurities is lacking. The objective of this thesis is to address this knowledge gap, with specific focus on increasing the Fe tolerance of a common automotive sheet alloy (AA6022) through modifications in composition and thermomechanical processing schedule. Towards this end, this thesis will strive to specifically evaluate the following hypotheses:

1. Decreasing the Si-to-Mg ratio within the required bounds for AA6022 will reduce the effect of increased Fe content on alloy formability
2. Increasing the degree of cold work will reduce the effect of increased Fe content on alloy formability

1.3 Organization of Thesis

To address these questions, the thesis is organized as follows. Chapter 2 details the alloys and thermomechanical processing approaches used in this study and provides an overview of the methods and analyses used to evaluate alloy microstructure and mechanical properties. The results of these experiments are reported in Chapter 3 and then discussed in the context of the preceding research questions in Chapter 4. The primary conclusions of the thesis and suggested future research directions are then outlined in Chapters 5 and 6, respectively.

2.0 Methods

2.1 Materials

A total of eight different combinations of alloy bulk composition, trace Fe content, and cold work level were evaluated in this study; each combination is documented in Table 2 below. Two nominal bulk compositions were evaluated, with each being similar to that of AA6022 but with different Si-to-Mg content ratios. Each alloy composition was then doped with either a high or low amount of trace Fe. Low Fe range was below 0.15 wt %, while the high Fe was between 0.15 and 0.20. The changes in Si:Mg ratio and Fe content were selected to evaluate formability and sustainability. Regarding the former, a higher Si:Mg ratio should increase the precipitation of Mg_2Si , resulting in increased strength, but reduced ductility [22, 27, 29]. As such, since Alloy 1 contains an increased Si:Mg ratio, it is expected that this alloy will have a higher predicted strength, but likely reduced formability relative to Alloy 2. It follows that Alloy 2 should have higher forming characteristics and be more scrap-friendly; however, it also is predicted to potentially develop Luder lines, which are undesirable in sheet product [41]. Each alloy/Fe content combination was then studied at two different cold work levels (~65% and ~81%), which were suggested by the design of experiments run in JMP, a statistical analysis software developed by the SAS Institute. The levels selected represent one or two passes on the cold mill and are commonly used cold work values.

Table 2: Overview of tested alloys' characteristics in wt %

	Fe	Si:Mg	Cu	Mn	Cr	Ti	Zn	% CW
A1_65CW_LF	low	1.41	0.13	0.07	0.03	0.03	0.007	65
A1_65CW_HF	high	1.42	0.13	0.07	0.03	0.03	0.005	65
A1_81CW_LF	low	1.41	0.13	0.07	0.03	0.03	0.007	81
A1_81CW_HF	high	1.42	0.13	0.07	0.03	0.03	0.005	81
A2_65CW_LF	high	1.05	0.13	0.07	0.03	0.02	0.004	65
A2_65CW_HF	low	0.99	0.12	0.07	0.03	0.02	0.004	65
A2_81CW_HF	high	0.99	0.13	0.07	0.03	0.02	0.004	81
A2_81CW_LF	low	1.05	0.12	0.07	0.03	0.02	0.004	81

Given the number of variables involved for a given sample, the following nomenclature is adopted for identifying each condition: A(alloy number)_(% CW)CW_(high or low)F. For example, the Alloy 1 condition with low Fe that underwent 81% cold work and low Fe is designated as A1_81CW_LF. The nominal composition for AA6022 is reported in Table 3 below for reference:

Table 3: Nominal AA6022 chemical composition (wt %)

	Si	Fe	Cu	Mn	Mg	Cr	Zn	Ti
AA6022	0.8-1.5	0.05-0.20	0.01-0.11	0.02-0.10	0.45-0.7	0.10	0.25	0.15

2.2 Processing

For this study, two ingots of each bulk alloy composition and Fe content combination (8 total ingots) were cast at Arconic Tennessee Operations with dimensions of 250" x 70" x 14" (6.35 m x 1.78 m x 0.36 m). Once casting was completed, the targeted composition listed for each respective ingot found in Table 3 was confirmed via quantometer sparking per ASTM E1251 [42]. The ingots were then scalped to remove the surface layer and square the edges; this step is done because the surface layer contains porosity and large constituents that would degrade alloy

performance and formability. After the scalping step was completed, each ingot underwent a multi-step thermomechanical process to produce the final sheet form evaluated in this study. A generalized schematic documenting a typical thermomechanical process for Al sheet is shown in Figure 4.

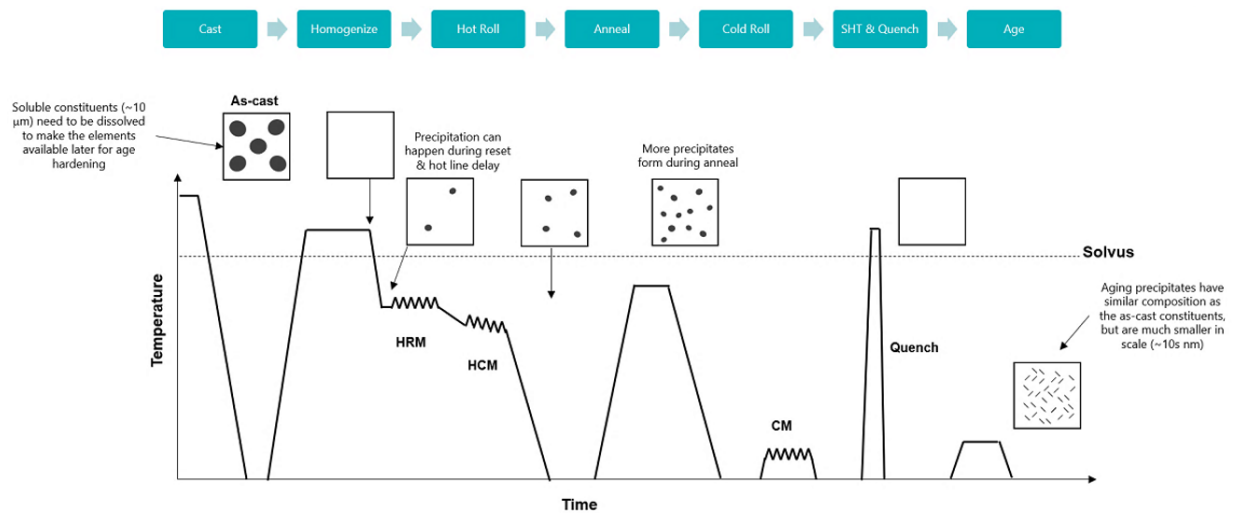


Figure 4: Overview schematic of typical thermomechanical processing steps for automotive Al sheet.

To track the temperature of each ingot during thermomechanical processing, thermocouples were inserted into small holes drilled into each ingot after scalping was completed. The ingots were then loaded into a preheat/homogenization furnace, where they were heated to a temperature above the solvus ($\sim 540\text{ }^{\circ}\text{C}$) for 18-20 h. This step is important for subsequent rolling treatment as it dissolves soluble particles, transforms insoluble particles, and limits microsegregation [43].

Once homogenized, the ingots were then hot rolled on a reversing roughing mill (HRM step in Figure 4) that reduces the ingot thickness. The slab is then transferred to a continuous mill (HCM in Figure 4), where it is rolled to near-final sheet thickness (generally less than 0.25”). Throughout the hot rolling schedule, preferred grain orientations develop that affect the alloy’s mechanical properties; this effect is mitigated by performing a brief intermediate anneal at a

temperature between 315 to 480 °C that induces recrystallization. A schematic of how the grain structure evolves throughout the thermomechanical processing is shown in Figure 5 below.

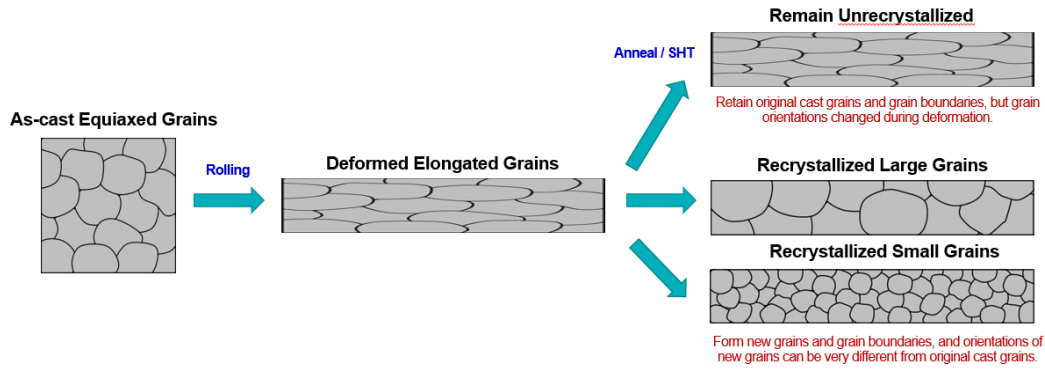


Figure 5: Schematic of typical grain structure evolution during thermomechanical processing of Al sheet alloys.

Once the intermediate annealing step is completed, the sheet is then cold-rolled (CM in Figure 4) to the final thickness. After reaching final thickness, the sheet is then run through a continuous heat treatment furnace for a solution heat treatment (typical time and temperature for this treatment are less than 10 min and > 540 °C) that dissolves any formed precipitates, followed by a spray quench. Samples were sheared into smaller sections for easier storage and transportation. The material then undergoes natural aging as it sits in the warehouse; OEM requirements mandate assessing material properties at 30, 90, and 180 d of natural aging. As such, samples were collected from each processed ingot at these times for analysis and characterization.

2.3 Microstructural Characterization

For each alloy condition, the microstructure was analyzed both in the F temper (as finished; or after the solution heat treatment step prior to natural aging) and as a function of natural aging time. Microstructure characterization was performed on full thickness longitudinal cross-sections

(examining the longitudinal-short transverse plane; L-ST) prepared from each alloy/aging condition. Additional details are provided in the following sections.

2.3.1 Metallographic Preparation

Metallographic samples were mounted in thermoplastic resin (similar to Lucite) using a mounting press that applied heat and pressure to cure the resin. Mounted samples were then prepared for microstructural characterization via iterative mechanical polishing and electro-etching per ASTM E3 [44]. A typical polishing procedure used in this study is provided in Table 4 below:

Table 4: Metallographic sample preparation procedure

STEP	ABRASIVE/CLOTH	FORCE	RPM	TIME
1	120 Grit SiC paper	10 N	300	until planed
2	320 Grit SiC paper	10 N	150	30 s
3	600 Grit SiC paper	10 N	150	30 s
4	3 μm /silk	25 N	150	3 min
5	3 μm / mol	20 N	150	2 min
6	1 μm / silk	25 N	150	3 min
7	1 μm / mol	20 N	150	2 min
8	0.05 μm OPS colloidal silica	25 N	150	30 s

Once the polishing procedure was completed, the as-polished samples were evaluated to determine constituent particle size distributions and morphology. Since the electro-etching will selectively attack regions of the microstructure, imaging this condition also permits examination of the general microstructure for each sample. After the as-polished imaging was completed, the samples were electro-etched with Barker’s reagent (HBF₄). During the 90 second etch, 35 volts

were applied to the samples [45]. This process both etches the sample to highlight grain structure, but also removes any residual near-surface damage induced during the mechanical polishing, thereby making the surface highly suitable for electron backscatter diffraction (EBSD).

2.3.2 Optical Microscopy and Analysis

Optical micrographs were captured for each alloy/aging condition combination in both the as-polished and electro-etched state using a Zeiss Z2m microscope with a motorized stage and Zeiss Zen imaging software. Typically, microstructure was captured at 50x and 200x magnification; an example micrograph is shown in Figure 6 below. These images qualitatively captured the typical size and distribution of Mg_2Si and Al-Fe-Si particles. Optical images for the electro-etched condition were only captured at 50x. Analysis of the full sheet thickness was performed by stitching images together to form a single file via Zeiss Zen software.

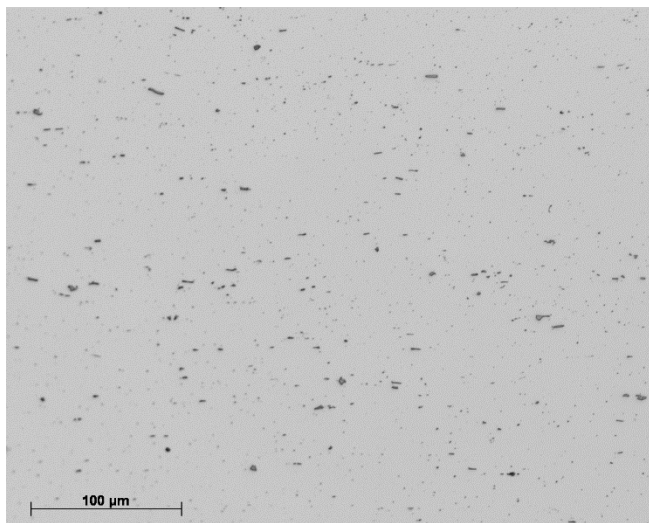
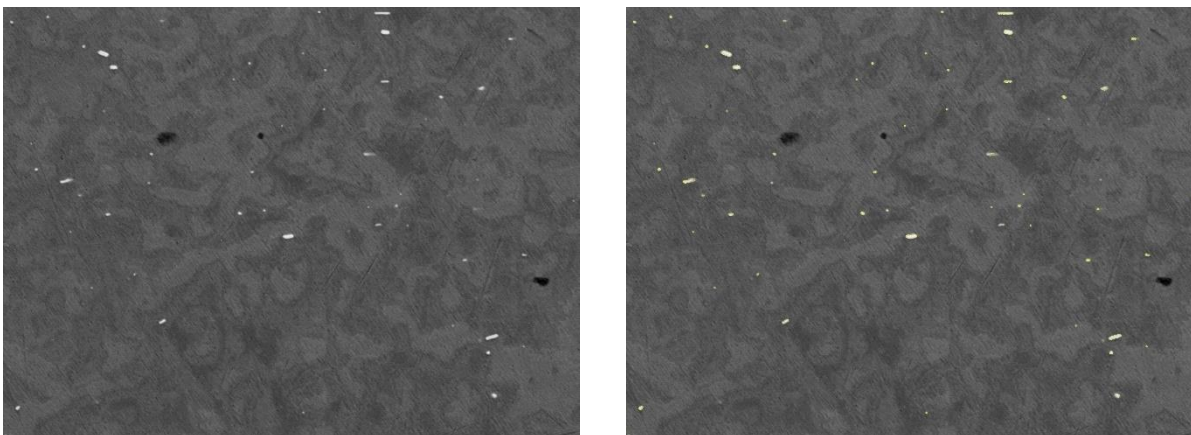


Figure 6: Typical optical image of the microstructure; original magnification was 200X

2.3.3 Electron Microscopy and Analysis

Electron microscopy-based analyses were performed using an FEI Apreo S scanning electron microscope (SEM). Cross-sectional analysis of smaller secondary phase particles was

performed on each alloy condition by collecting a series of twelve images captured at 5000x; this resulted in approximately 700-900 individual particles for subsequent analyses. X-ray energy dispersive spectroscopy (EDS) point scans were performed on a random subset of particles from each condition to identify their nominal composition. Image segmentation and analysis was conducted using Mipar software. Images of before and after segmenting are shown in Figure 7.



Before segmentation

After segmentation

Figure 7: SEM images before and after segmentation.

As shown in Figure 7, the white particles (Al-Fe-Si) are outlined in yellow during segmenting. Parameters such as area, density, length, and width were collected and analyzed to produce average size and f/r measurements, where f is the fraction of particles and r is the particle radius.

The grain structure and texture for each condition was assessed via electron backscatter diffraction (EBSD) over the entire cross-section thickness; individual maps were stitched using the montaging capability of the EDAX software. Relevant parameters for these scans include a specimen tilt of 70° , step size of $0.8 \mu\text{m}$, accelerating voltage of 20 keV, and probe current of 51 nA. Analysis of the data included the calculation of the grain size and determination of texture parameters using EDAX software that leverages standardized methods of evaluation. For example,

the grain size from EBSD data is determined using ASTM E2627 [46], which is similar to the linear intercept method used in optical metallography [47].

2.4 Mechanical Property Evaluations

2.4.1 Uniaxial Tensile Testing

To assess the mechanical properties of each alloy condition as a function of natural aging time, uniaxial tensile testing was conducted according to ASTM E8 [48] using a servohydraulic load frame and an attached extensometer. Specimens were machined directly from the sheet using a milling machine and had a rectangular gauge cross-section with thickness equal to the sheet thickness and a width of ~18 mm. The overall specimen length was ~280 mm, but the gauge section was 57 mm in length. Specimens were tested with the loading axis parallel to the long transverse direction (LT), longitudinal direction (L), and at a 45° angle from the L direction of the rolled sheet. For most properties, only the LT data are utilized as is required by current OEM specification.

Specific properties of interest from the tensile data include yield strength, ultimate tensile strength, elongation to fracture, strain hardening exponent (n-value), and Lankford coefficient (r-value). Yield strength was determined using the 0.2% offset, while the elongation to failure and ultimate tensile strength were determined from the maximum elongation and stress values measured during the experiment. The second two parameters, n-value and r-value, were determined using the work-hardening regime of the stress-strain response; an example of a typical engineering stress-engineering strain curve for AA6022-T4 with this regime highlighted is shown in Figure 8. The strain hardening exponent is determined by fitting the work hardening regime to the Hollomon power law equation, $\sigma = K\varepsilon^n$, where σ is the true stress, ε is the true plastic strain, and K is the strength coefficient. As such, the strain hardening exponent can be determined from

the slope of the true stress-true plastic strain curve and is useful because of its theoretical equivalence with the true strain for the onset of necking [49]. For the current study, the n-value was fit over the strain interval from 10-20% rather than over the entire curve. Regarding the Lankford coefficient (r-value), this metric describes the resistance of a material to thin and is often referred to as the plastic strain ratio given that it is calculated from the quotient of the true width strain and true thickness strain, $r = \frac{\epsilon_w}{\epsilon_t}$ [50]. Since the r-value inherently depends on strain measurements from different directions, the reported value is an aggregate of the results from the LT, L, and 45°-oriented experiments. Additionally, since the dimensions of the sample are required for the analysis, this metric was only evaluated at a constant strain level of 10%.

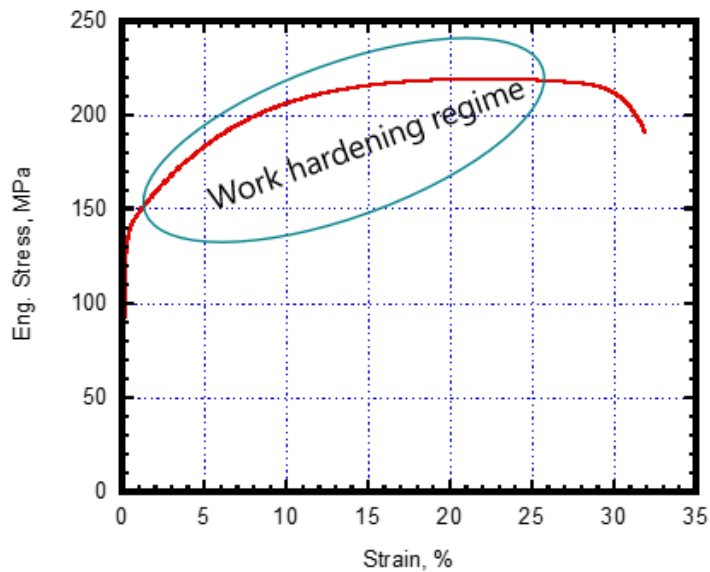


Figure 8: Typical stress-strain curve for AA6022-T4, with work hardening regime indicated.

2.4.2 Formability Testing

Two types of formability evaluations were performed in this study: flat hems and Verband der Automobilindustrie (VDA) bend testing. The latter is instrumented, allowing for a quantitative measurement of formability, while the former only offers a qualitative metric rating, but is an actual hemming process. Experiments were conducted in either the L or LT direction; L tests are

bent perpendicular to the rolling direction, or a transverse bend axis, and LT are parallel with the rolling direction, or a longitudinal bend axis. As with the uniaxial mechanical properties, specimens from each alloy condition were evaluated after 30, 90, and 180 d of natural aging.

Briefly, the VDA test is a three-point bending experiment that uses digital image correlation to measure strain throughout the bend as well as the angle of the bend angle, α (Figure 9) [51]. Additionally, since the strain is recorded in-situ, the plane strain fracture limit can be identified at the onset of cracking. The bend angles measured before cracking are compared with bend angles of known acceptable samples and a correlation exists between the bend angle, α , and the applied plane strain. For this experiment, four square sheet specimens with side length of 60 mm are tested per alloy condition and direction. A schematic of the VDA test setup is shown in Figure 9 and is composed of a thin punch that presses on the sheet specimen as it lies on two rollers with a known gap. During the experiment, the thin punch applies pressure to the sample using a mechanical loading frame, resulting in the sample deforming into a V-shape as the punch pushes the material into the roller gap. The primary metric utilized in this study was the bend angle α , with higher values of α suggesting improved formability. Other relevant parameters for testing include a 0.5 mm roller gap and a 0.2 mm punch tip radius.

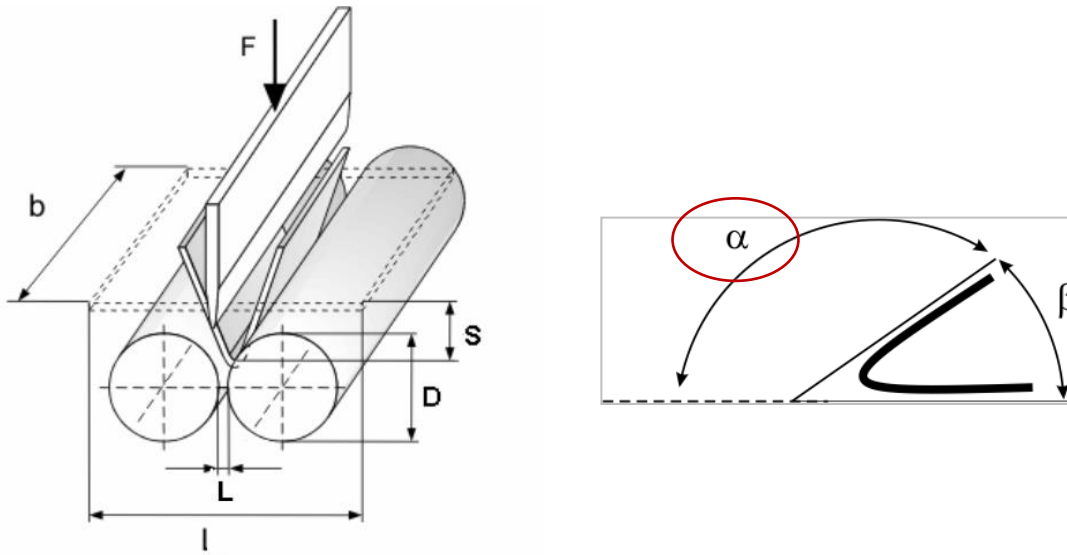


Figure 9: Schematic of the (left) VDA setup and (right) bend angle [52] Reprinted from VDA 238-100, Verband der Automobilindustrie, Plate bending test for metallic materials, Copyright (2017), with permission from Verband der Automobilindustrie

To directly evaluate the hemming performance of the different alloy conditions, flat hemming experiments were performed as a function of natural aging time using similar 60 mm-square sheet specimens. Four hem samples were performed per alloy condition and natural aging time with the hem axis oriented both parallel and perpendicular to the L direction (so tested in L or LT). The nominally setup for the flat hem test is similar to that of the VDA experiment, as shown in Figure 10, with the key differences being that the hem test is not instrumented and proceeds until a complete 180° hem has been performed.

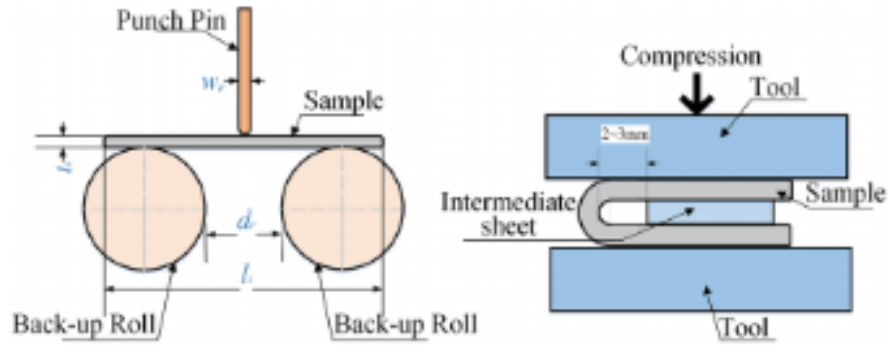


Figure 10: Flat hem testing schematic [55] Reprinted from Automotive Innovation, H Lu, J. Zhang, N. Tian, X. Song, M. Ma, G. Lu, Recycle-Friendly Aluminum Alloy Sheets for Automotive Applications Based on Hemming, Copyright (2018), with permission from Springer Nature

Once the test is finished, the hem is visually examined and then qualitatively rated according to a 1-5 scale, where 1 indicates minimal evidence of surface rumpling (orange peel) or cracking and 5 represents severe surface cracking present. Examples of each rating are shown in Figure 11. In general, a score of 2 or higher is widely considered acceptable while a score of 3 may be considered passable depending on OEM specifications. However, given the qualitative nature of this assessment, it is common for some variation in ranking to exist from operator to operator, which can make marginal cases challenging to evaluate.

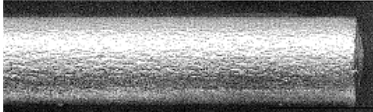
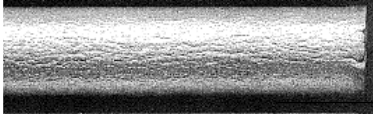
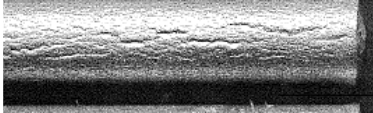


	Rating Number	Description	Category
	1	Zero to moderate orange peel	Acceptable Hem
	2	Severe orange peel	Acceptable Hem
	3	Cracks visible with 3X magnification	Marginal
	4	Cracks visible without magnification	Unacceptable
	5	Fracture/continuous crack along bend	Unacceptable

Figure 11: Typical ranking criteria used to evaluate hems

3.0 Results

3.1 Microstructure Evaluation

3.1.1 Secondary Phase Particles

Since the subsequent evaluations are performed on naturally aged specimens, it is important to ensure that the solution heat treatment was effective at re-solutionizing any Mg_2Si particles that were nucleated during the thermomechanical processing steps. Overview micrographs taken with a scanning electron microscope for each tested condition after the completion of the solution heat treat and quench step are shown in Figure 12. Scalebar is 100 μm . Two features are readily apparent: (1) the equiaxed grain morphology and (2) the presence of larger bright-white secondary phase particles, which were not returned to solution. Regarding the former, an equiaxed morphology is expected given the applied thermomechanical processing associated with forming sheet product [54]. Regarding the particles, this insolubility and large size indicates that these are unlikely to be Mg_2Si , which suggests that solution heat treatment step was effective at returning the strengthening precipitates back to solution. Interestingly, comparison of the various alloys reveals a limited influence of bulk alloy composition and cold work level on the distribution of the secondary phase particles. Instead, consistent with the likelihood that these are Fe-rich phases, the number density of the white particles appears to be tangibly increased with an increase in the Fe content.

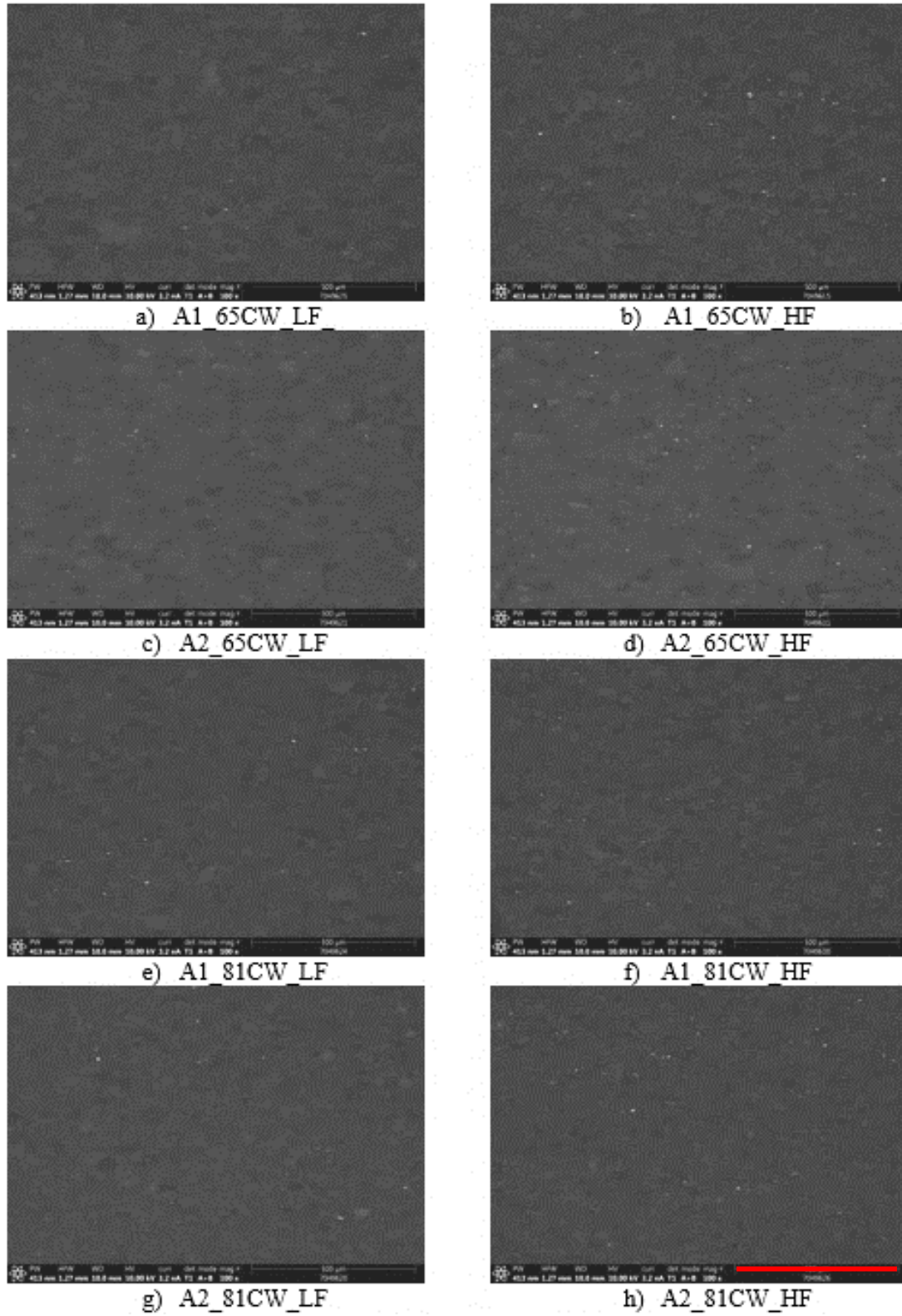


Figure 12: SEM backscatter electron images of each alloy microstructure after solution heat treat (scalebar is

100 μm)

Given the observed trend of increasing particle frequency with increasing Fe content, as well as the apparent insoluble nature and random distribution of the particles, it is likely that these particles are Fe-containing constituents. To confirm this, point EDS scans were performed on selected particles (a representative micrograph of such particles from A2_65CW_HF is shown in Figure 13 below). Analysis of the EDS results demonstrate that the particles had an elemental composition distinct from the alloy matrix and are likely $\text{Al}_{12}(\text{Fe},\text{Mn})_3\text{Si}$.

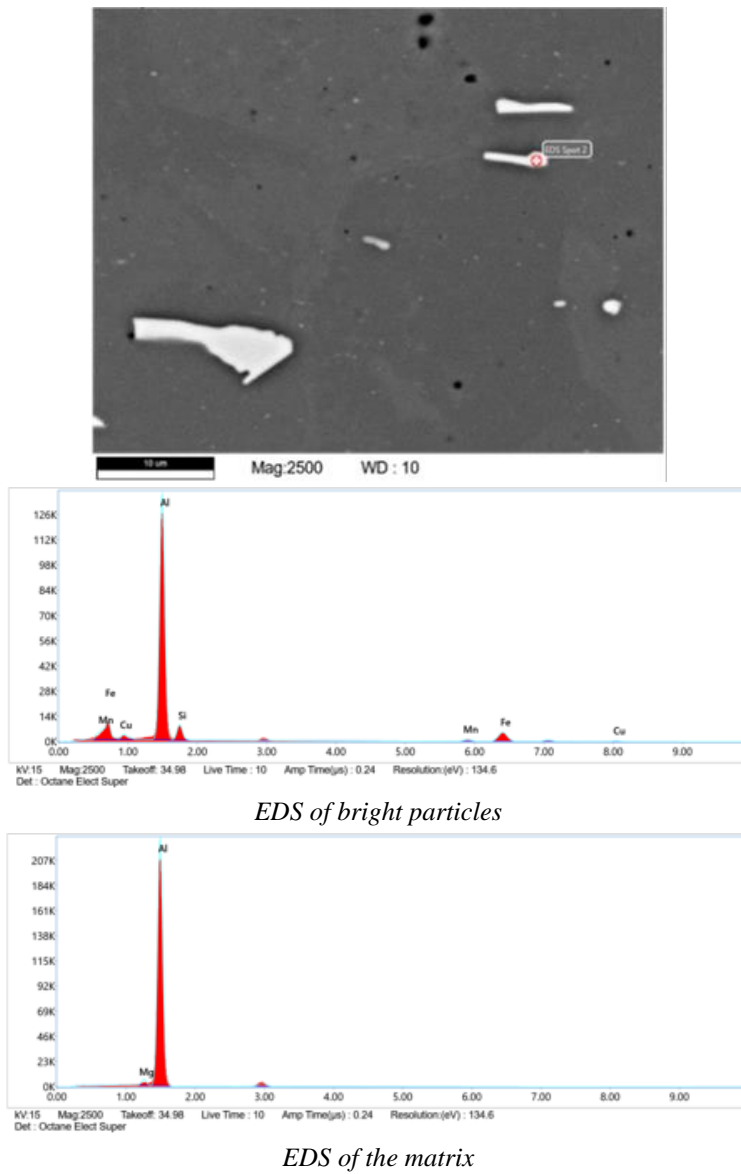


Figure 13: EDS of (middle) bright particles and (bottom) matrix region of the SEM micrograph (top)

3.1.2 Grain Structure

The grain structure for each condition was examined using both optical and scanning electron microscopy techniques, but this section will primarily focus on the results from the electron backscatter diffraction (EBSD) analysis. Inverse pole figure (IPF) maps of a full thickness cross-section (L-ST plane; ST is parallel to the vertical direction) for each of the eight tested condition are shown in Figure 14 below. Note that these data were collected after 8 d of natural aging, but are considered representative of the microstructure for all aging conditions given that natural aging does not change the grain morphology. Scalebar is 400 μm .

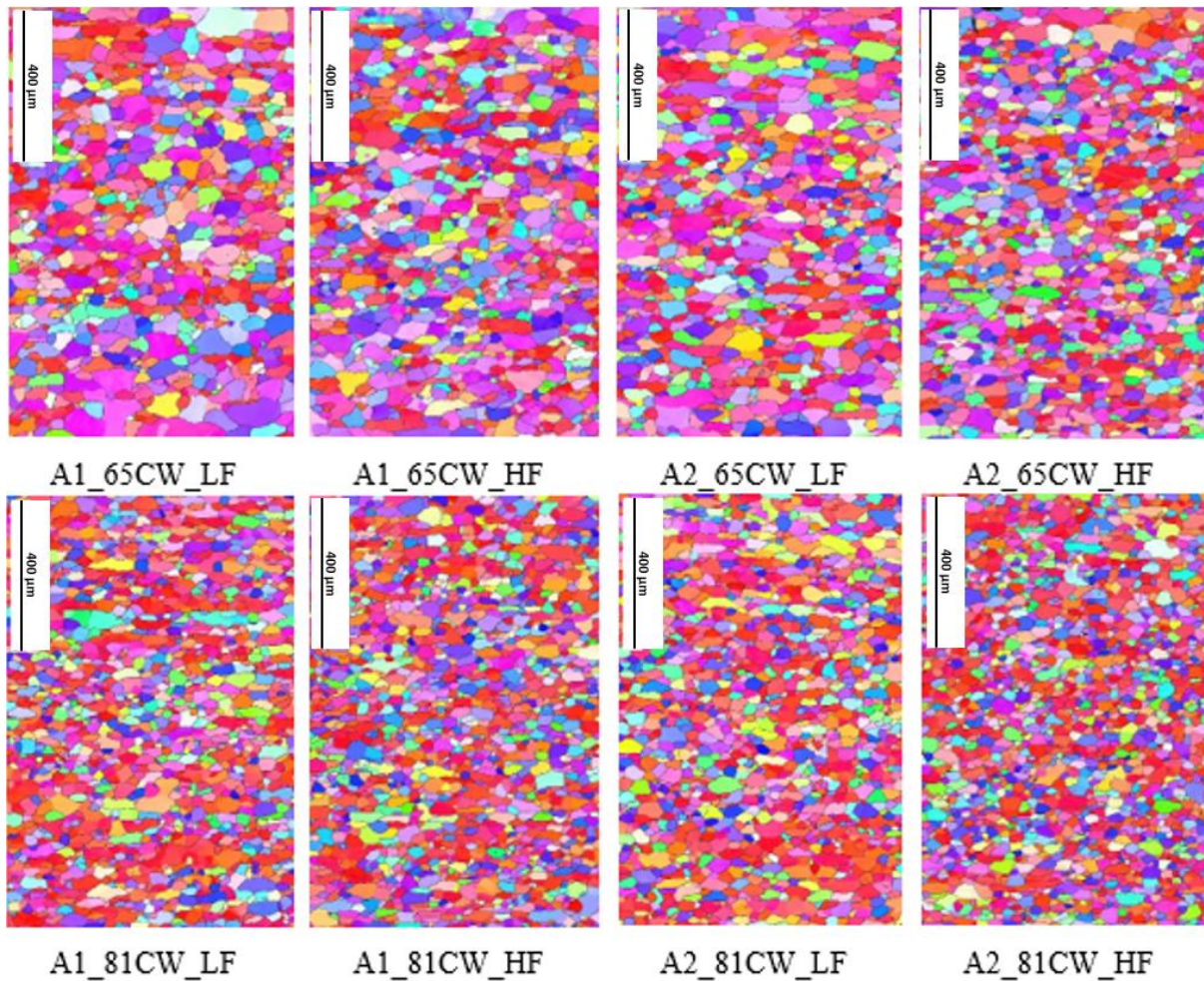


Figure 14: EBSD IPF maps of the eight evaluated materials

Four trends are notable from these IPF maps. First, as quantified by the average grain size in Table 5 below, a given bulk alloy composition and Fe level generally exhibited a larger grain size in the higher cold work conditions. Second, examination of the grain structure homogeneity throughout each cross-section revealed nominally consistent grain structure in the high cold work conditions. However, the near-surface regions of the low cold work alloys exhibited significantly larger grains than in the center of the sheet, with the difference being particularly acute for A1_65CW_LF. This variation is quantitatively provided by the data in Table 5. Third, the average grain size data for the bulk regions also indicates a potential role of Fe content, with the higher Fe content alloys (for a constant bulk composition and cold work level) consistently having a smaller average grain size. Lastly, a similarly consistent behavior is also noted between the two bulk alloy compositions, with Alloy 1 generally having a larger grain size as compared to Alloy 2 for a constant Fe content and cold work level.

Table 5: Bulk and surface grain size for each alloy

	Grain Size (um)	
	bulk	surface
A1_65CW_LF	48	105
A1_81CW_LF	35	47
A1_65CW_HF	41	47
A1_81CW_HF	32	36
A2_65CW_LF	40	46
A2_81CW_LF	33	34
A2_65CW_HF	36	43
A2_81CW_HF	30	33

As the above data suggests a role of Fe content on the grain size, this potential influence can be further evaluated by comparing the f/r (f : fraction; r : average radius) calculated from the images in Section 3.1.1 to the average grain size reported in Table 5. These data are plotted in

Figure 15 below, which indicates that as f/r increase, the average grain size is generally decreasing. Such results suggest a potential influence of the Fe-bearing constituent particles on pinning the grain boundaries (e.g., Zener pinning), consistent with the observation of the higher Fe content alloys generally having a smaller grain size than the low Fe content alloys.

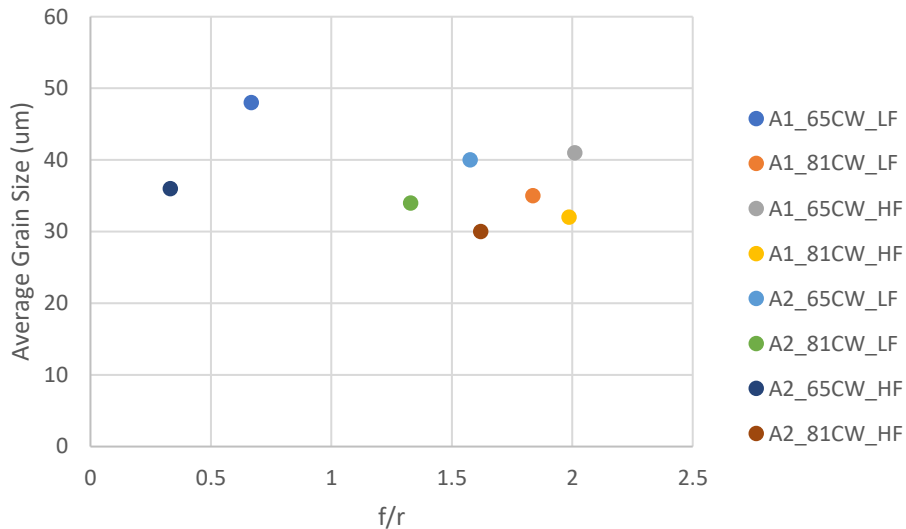


Figure 15: Effect of f/r on the average grain size for each tested alloy condition.

In addition to providing insights into the grain size and spatial distribution of the grain structure, EBSD also can provide insights into the texture developed in each alloy condition. Given the extent of thermomechanical processing necessary to produce aluminum sheet, it is expected that preferential textures will develop in these alloys, particular the cube or $\{001\}\langle 100 \rangle$ texture. Given that texture reflects the extent of preferred crystallographic orientation, it will have significant impacts on the downstream mechanical properties and formability of a given alloy, which motivates quantification of the fraction of grains with this specific texture component [54]. The results of this analysis for each alloy are shown in Figure 16. The number above the bars are the bulk grain size. Four primary observations are noted for these data. First, as expected given the increased extent of induced deformation, the high cold work condition consistently exhibits

larger fraction of cube texture than the same alloy (Fe content and bulk composition) in the low cold work condition. Second, while the differences are subtle and nearly within the reported error bars (standard error of the mean, calculated by dividing standard deviation by the square root of the sample size), it appears that increasing the Fe content in the low cold work condition resulted in slight increase in cube fraction for both bulk compositions. Third, considering the high cold work conditions, there was a minimal effect of Fe content in Alloy 1, but a significant increase (~50%) in cube texture fraction for the high Fe content condition of the high cold work variant of Alloy 2 relative to the low Fe content condition. Lastly, smaller grain sizes generally resulted in higher cube texture fraction.

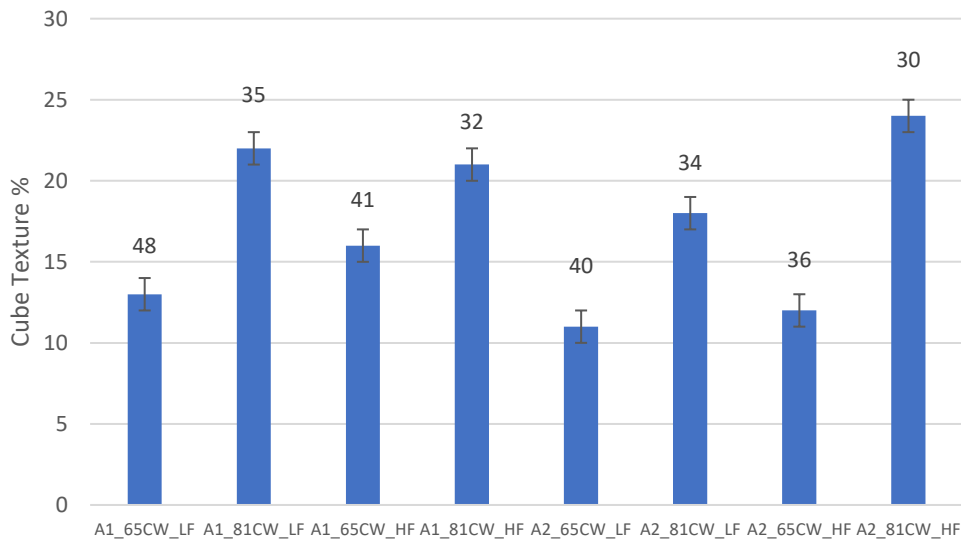


Figure 16: Variation in fraction of grains with cube texture for each condition. The number above each bar indicates the average grain size for that respective alloy condition (in micrometers) and the error bars correspond to the standard deviation of multiple measurements.

3.2 Mechanical Testing Results

Given that a key OEM requirement is the yield strength after various natural aging times, uniaxial tensile experiments were performed as a function of natural aging time (up to 270 d) for each condition of interest. The measured tensile yield strength (TYS) versus natural aging time relationships for each alloy condition for specimens oriented with the loading axis parallel to the LT direction of the sheet are shown in Figure 17. Iso-yield strength lines corresponding to the OEM-allowable maximum yield strength after 30, 90, and 180 d are also plotted for reference [55]. Regarding the influence of natural aging time, all alloys exhibited an initially steep increase in yield strength up to 30 d, followed by a gradually shallower increase as natural aging time increased to 270 d. Such behavior is consistent with the broadly reported trends for 6xxx-series Al alloys [43]. Interestingly, while a spread in yield strength is observed across the eight tested alloy conditions (as expected given the differences in thermomechanical processing and alloy composition), the relative ordering of the yield strength changed minimally with aging time. For example, the high and low cold work versions of the low Fe-bearing Alloy 1 variant consistently exhibited the highest yield strengths. Similarly, the high and low Fe-bearing versions of the low cold worked Alloy 2 variation consistent had the lowest yield strengths. Critically, all tested conditions did meet the governing OEM specifications, indicating that the developed alloys could be utilized in-service.

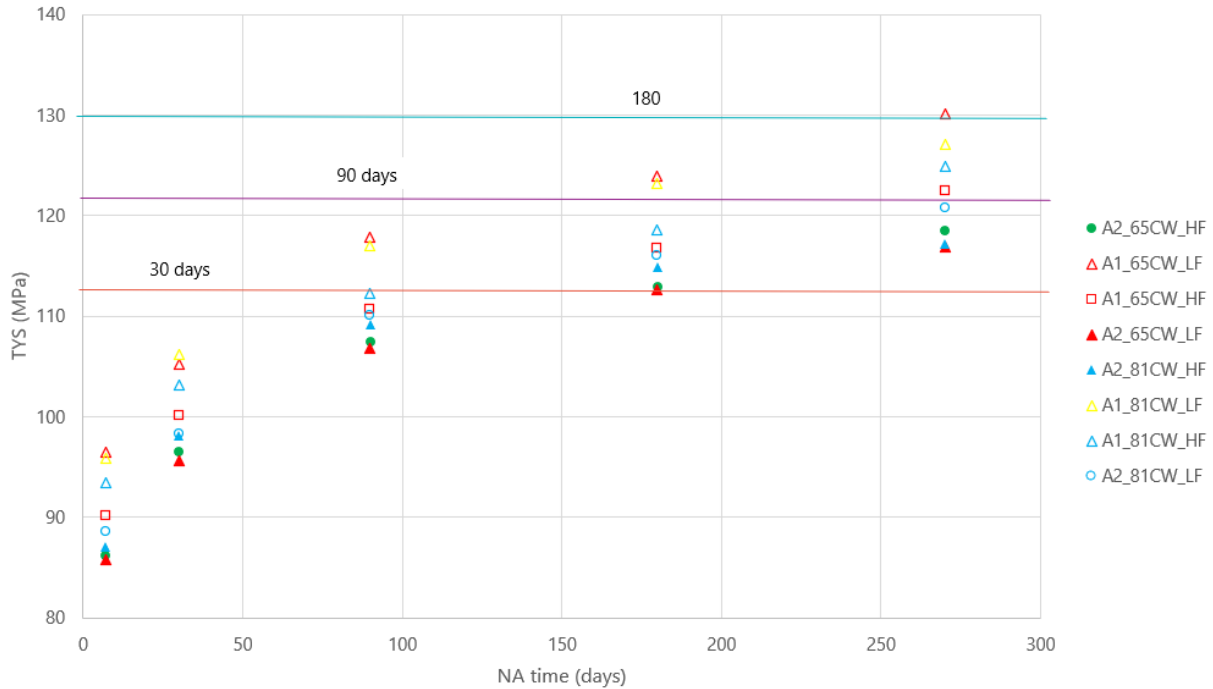


Figure 17: Tensile yield strength as a function of natural aging time. The lines correspond to OEM-mandated maximum values at 30, 90, and 180 d.

Due to the importance of the yield strength at 30, 90, and 180 d for qualifying material for use in automotive sheet applications, the data from Figure 17 are replotted in Figure 18 to enable easier comparison of trends. In particular, these data demonstrate that Alloy 1 consistently exhibited an increased yield strength for a given condition relative to Alloy 2, indicating a potential role of Mg:Si ratio. Beyond that, there appears to be limited correlations between the extent of cold work or the Fe content, with the factors causing increases in yield strength for one condition leading to decreases in yield strength for another (*e.g.*, effect of cold work for the low Fe-bearing versions of Alloy 1 and Alloy 2).

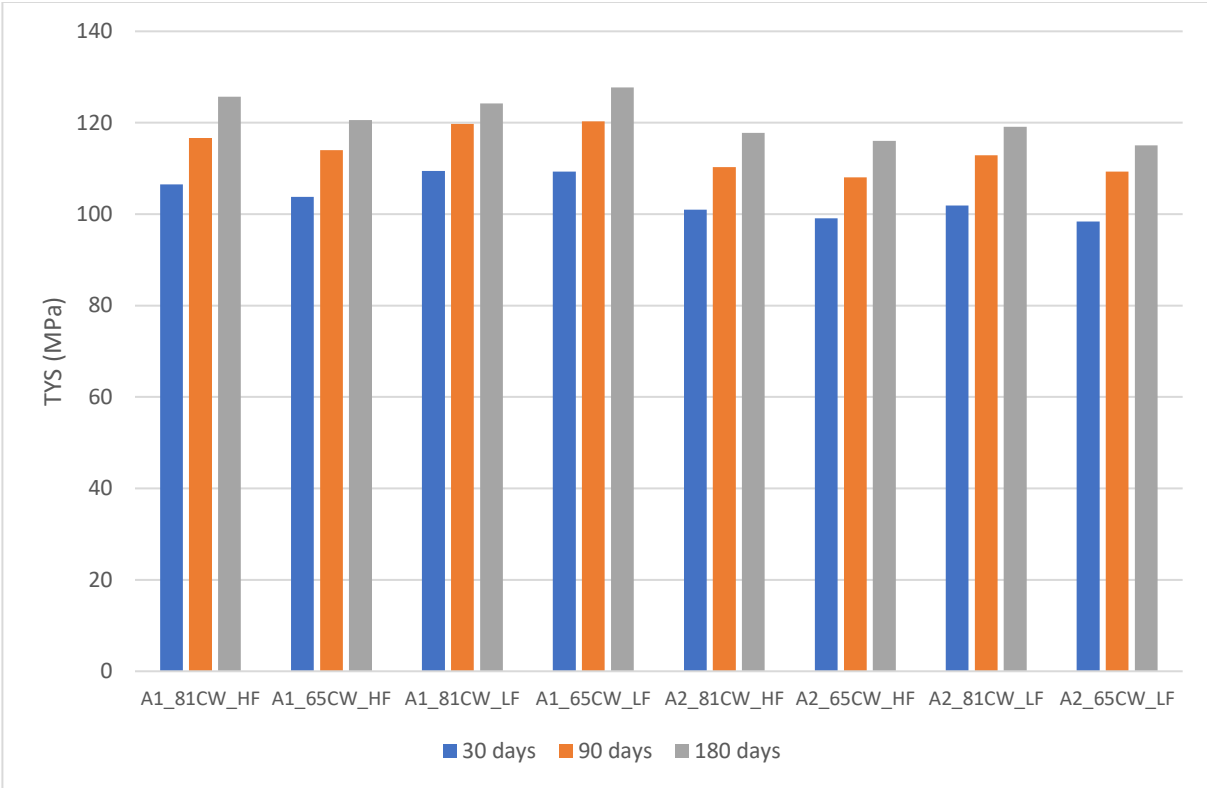


Figure 18: Yield strength after 30, 90, and 180 d of natural aging for each alloy

A proxy for formability that can be obtained from the stress-strain curve is the strain hardening exponent (n), which can be shown to equal the true strain at which plastic instabilities occur (*i.e.*, necking). To understanding how this parameter varied with alloy condition and natural aging time, the measured stress-strain relationships were fit to the Holloman relationship ($\sigma = K\varepsilon^n$) over the strain range from 10-20% to obtain the value of n . The results of this fitting are shown in Figure 19 below; examination of these data indicate that the overall differences in calculated n are relatively small, spanning from ~ 0.235 to 0.25 , across the tested alloy conditions.

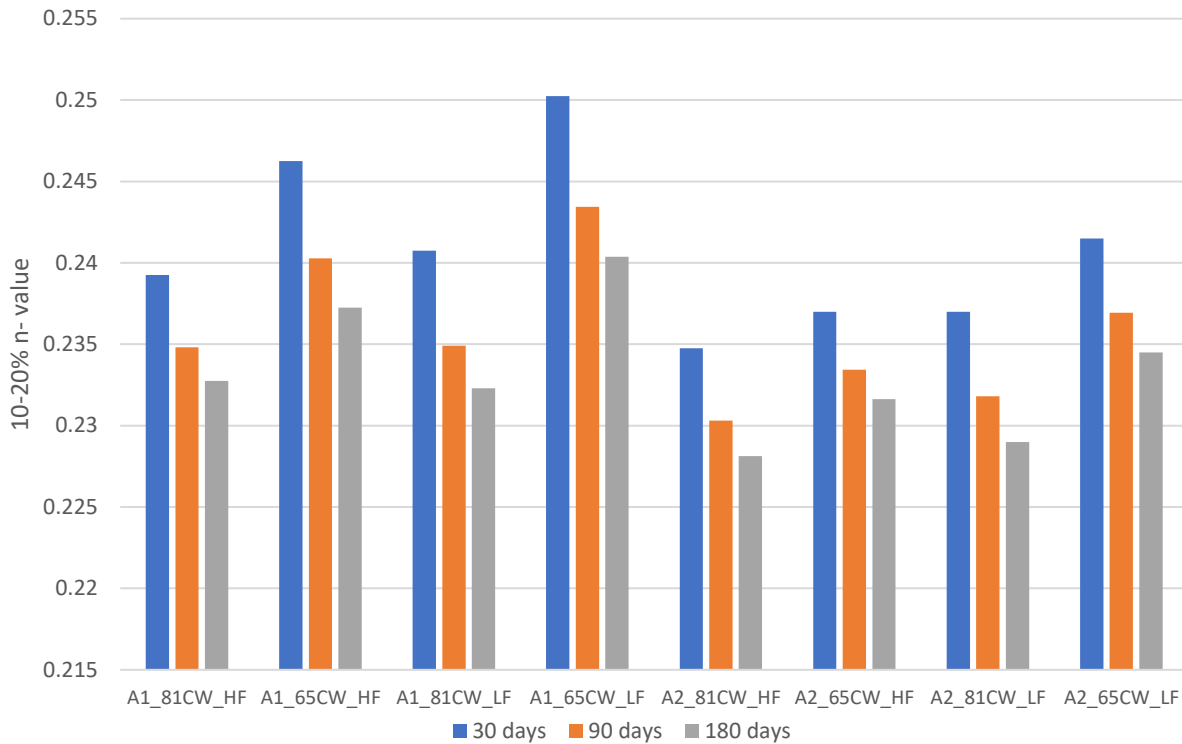


Figure 19 Effect of natural aging kinetics on the strain hardening exponent (from 10-20% strain) for each tested alloy condition.

However, four trends do appear consistently in the dataset. For all tested alloy conditions, a consistent decrease in n is observed as the natural aging time increases; such behavior is consistent with expectations for an increasing yield strength noted in Figure 17 (which typically correlates with reduced ductility). However, it is interesting to note that, despite having a consistently higher yield strength (Figure 17), Alloy 1 regularly exhibits a higher strain hardening exponent for a given Fe content and cold work level as compared to Alloy 2. The third notable trend is that for a given bulk alloy composition and cold work level, increasing the Fe content generally led to a reduction in the strain hardening exponent. Lastly, increasing the cold work level for a constant bulk alloy composition and Fe content also resulted in decreases in the n value.

Figure 20 shows the measured n-value between 10-20 % strain after 180 d of natural aging when strain parallel to the L, LT, and 45° from the L direction. Several observations are notable from these data. First, it is interesting to note that the strain hardening exponent was highest at a 45° angle, with the n-value along the L direction always being the lowest. Second, for a given Fe content and cold work level, Alloy 1 exhibited higher n values across all tested directions. Third, decreasing cold work extent generally led to an increase in n-value for a given Fe content and bulk alloy composition when strained parallel to the L or LT directions; the n-value decreased with decreasing cold work when tested at a 45° angle in the L-LT plane. Lastly, the effect of Fe content had a complex dependence on direction of testing and cold work.

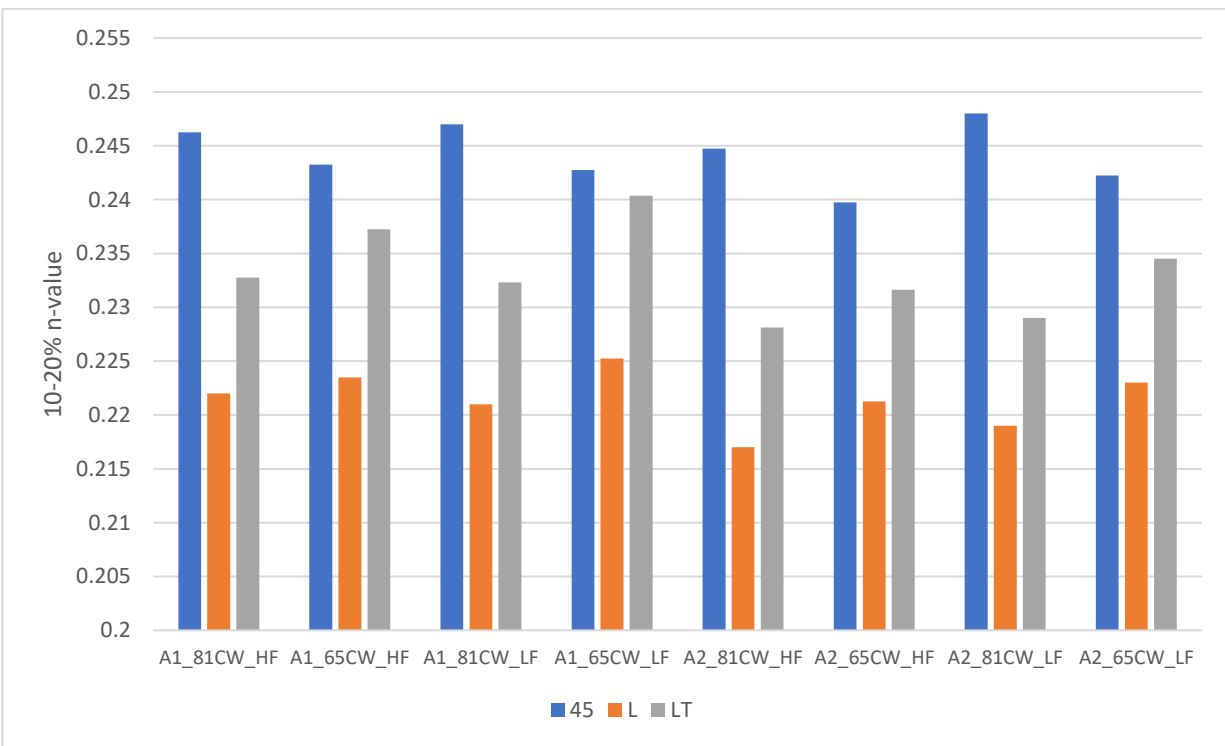


Figure 20: Variation in n-value (10-20%) as a function of loading direction after 180 d of natural aging

To assess each alloy condition’s resistance to thinning, the Lankford coefficient (*i.e.*, r-value; defined as the quotient of the true width strain and true thickness strain) [50] was assessed after 10% elongation; note that a higher r-value correlates with improved deep drawability. The

results of this analysis as a function of natural aging time for specimens oriented with the loading axis parallel to the LT direction of the sheet are shown in Figure 21. Four observations are notable from these data. First, increasing the level of cold work for a given Fe content and bulk alloy composition improved the resistance to thinning; specifically, the high cold work alloy variants generally exhibited an increase of >15% in r-value relative to same condition in the low cold work state. Second, Fe appears to have a limited influence on the measured r-value, with a given cold work and bulk alloy composition generally exhibiting the same behavior regardless of high or low Fe content. Third, while Fe content had an overall limited influence and minimal effect of bulk alloy composition was observed for the high cold work conditions, there is a notable increase (~8%) in the measured r-value for the low cold work variants of Alloy 2 relative to Alloy 1. Lastly, the measured r-value tended to slightly increase with natural aging time, though the extent of increase varied from condition to condition and was overall limited.

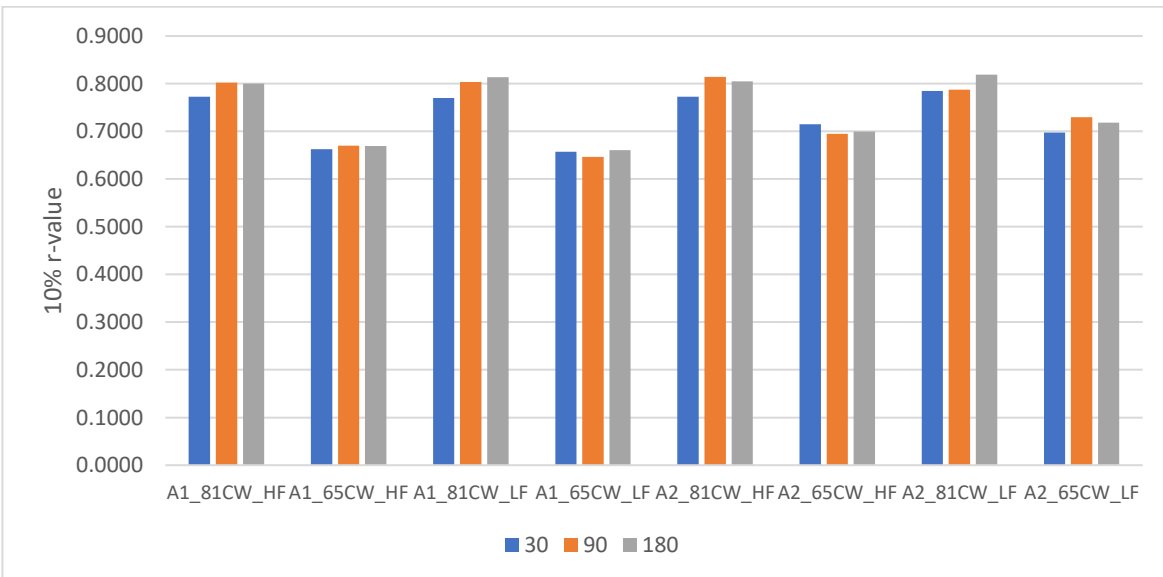


Figure 21: Measured r-value at 10% elongation for each alloy condition parallel to the L direction as a function of natural aging time.

In addition to informing the deep drawability, the r-value can also be used to quantitatively inform the material's ability to be deformed in the plane of the sheet. This can be determined through the calculation of the normal anisotropy ratio (r_m), which is determined from the measured r-values for specimens oriented with the loading axis parallel to (1) the LT direction of the sheet, (2) the L direction of the sheet, and (3) at 45° from the L direction of the sheet. The specific formula for this calculation is as follows [50]:

$$r_m = \frac{r_{LT} + r_L + 2r_{45}}{4}$$

The calculated r_m value for each condition after 180 day of natural aging is shown in Figure 22 below.

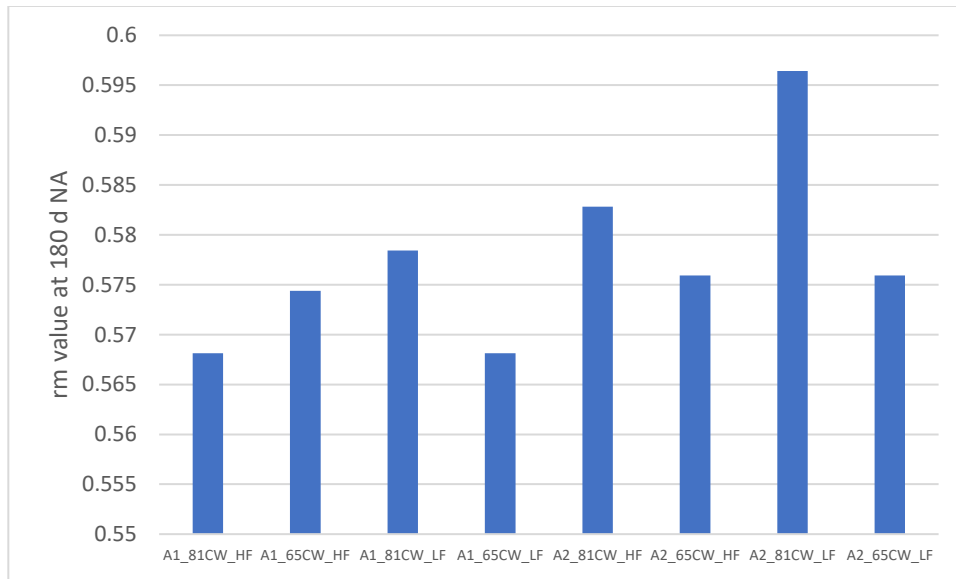


Figure 22: Measured r_m for each tested condition after 180 d of natural aging.

To get further insights into the role of directionality, the discrete r-values for each condition for specimens oriented parallel to LT, L, and 45° in the sheet plane at 10% elongation and 180 d of natural aging are shown in Figure 22. These results demonstrate the important effects of anisotropy on the thinning resistance of aluminum alloy sheet. Specifically, specimens oriented parallel to the L direction of the sheet exhibited the greatest thinning resistance, followed by the

samples oriented parallel to the LT direction, which had a generally modest reduction in r-value relative to the L direction. However, for all conditions, the specimens oriented at a 45° generally exhibited significantly reduced resistance to thinning (often 50% less than the L direction). While these nominal trends were observed across all tested conditions, there were three other notable observations. First, the alloys which had the highest r-value in the L direction (*e.g.*, A1_65CW_HF, A1_81CW_LF, A2_81CW_LF, etc., which also had the highest r-values in the LT direction) consistently had the lowest r-value in the 45° direction. Second, across both tested bulk alloy compositions, the 45° oriented specimens with high Fe content exhibited a higher r-value in the high cold work condition, while the low Fe content alloys had the higher r-value at the low cold work level. Third, this trend was exactly the opposite for the LT oriented specimens, with the high cold work level yielding the highest r-values for the low Fe alloy compositions and the low cold work level exhibiting the highest r-values for the high Fe content conditions.

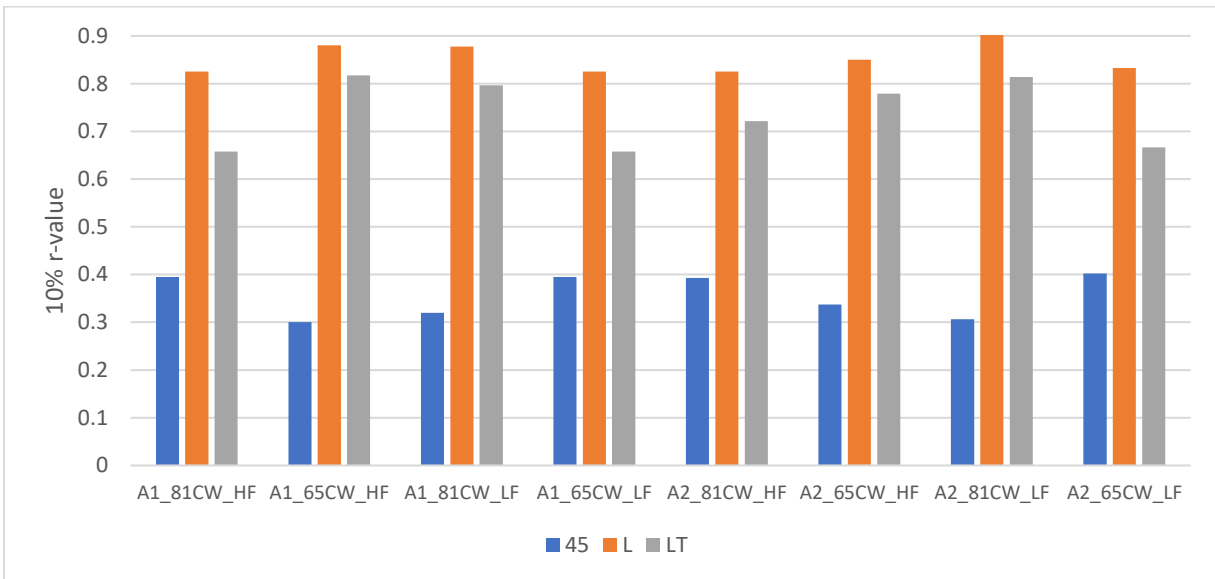


Figure 23: Measured r-value along the L, LT, and 45 directions for each alloy condition after 10% elongation and 180 d of natural aging.

3.3 Formability

The bend angles measured via VDA experiments on each evaluated alloy condition after 30, 90, and 180 d of natural aging are shown in Figure 23; the errors bars shown in Figure 23 correspond to the calculated standard deviation from four replicate measurements. Note that larger bend angles indicate increased formability relative to lower VDA-measured bend angles. Three observations are notable from these data. First, all tested alloys exhibit the same nominal relationship between natural aging time and VDA bend angle. Specifically, each condition has a maximum in measured bend angle at 30 d of natural aging, followed by a 15-17° decrease in bend angle (on average across all tested conditions) with an increase in natural aging time to 90 d. Interestingly, further increases in natural aging time to 180 d induces only minor additional decreases in bend angle, with several conditions in Figure 23 showing no decrease in bend angle between 90 and 180 d of natural aging. Such behavior is consistent with the results shown in Section 3.2, which noted an initially strong decrease in tensile ductility metrics with increasing natural aging time from 30 to 90 d, followed by limited declines with further natural aging.

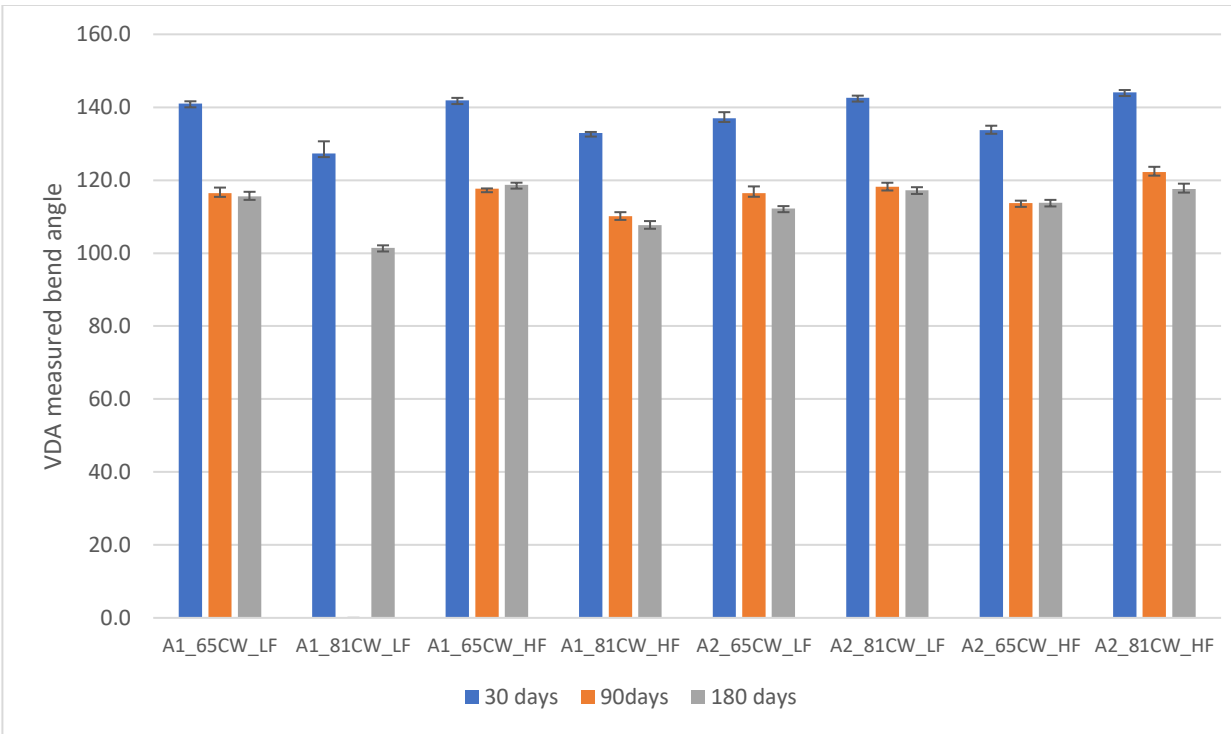


Figure 24: Measured bend angles via VDA testing for each alloy condition after 30, 90, and 180 d of natural aging. Note that error bars correspond to the standard deviation of multiple measurements.

Second, the results revealed opposite behaviors between the two bulk alloy compositions studied. For example, both the low and high Fe content conditions of Alloy 1 had the highest VDA bend angles after 65% cold work, while 85% cold work yielded higher VDA bend angles for Alloy 2, regardless of Fe content. Interestingly, except for Alloy 1 after 81% cold work, Fe content appears to have only a limited impact on the VDA bend angle, with the low and high Fe contents typically yielding bend angles with $\sim 5^\circ$ of each other. Finally, the alloy conditions with the highest VDA bend angles at 30 d of natural aging also generally had the highest VDA bend angles after 180 d of natural aging. Given the inherent long times required to make measurements after 90 and 180 d of natural aging, such results suggest that 30 d of natural aging could be used to enable higher throughput screening of potential alloys' formability.

3.3.1 Flat Hemming

While VDA bends provide quantitative measurements of formability, they do not fully replicate the demanding nature of the actual hemming process. As such, replicate specimens from each alloy condition underwent a flat hemming test, where the sample is folded into a 180° bend, followed by a qualitative optical evaluation guided by the ranking system shown in Figure 11 (Section 2.4.2). Images of the hem samples after 180 d of natural aging can be found in Figure 25 below.

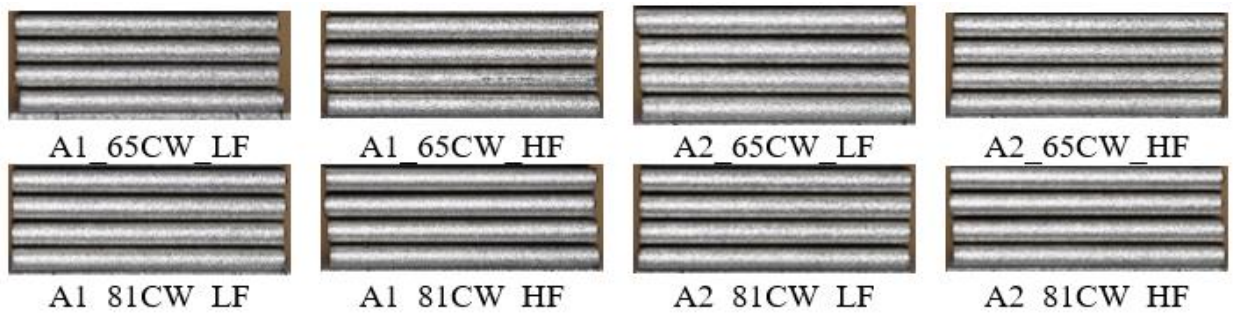


Figure 25: Images of the flat hem samples after 180 d of natural aging.

The results of these hemming experiments (performed with the bend line parallel to the L direction of the sheet) are shown in Figure 26 for each condition as a function of natural aging time (30, 90, and 180 d). Examination of these data reveal that most conditions were rated as a 2 (*i.e.*, acceptable) regardless of the natural aging time. However, three trends are notable from these data. First, on average, a given cold work and Fe content condition in Alloy 2 either exhibited similar or better performance relative to the analogous condition in Alloy 1, indicating a potential positive role of higher Mg:Si ratio. Second, for both alloy composition, the worst performing material was the low Fe, 65% cold work alloys, with the Alloy 1 and Alloy 2 variants having hem ratings of 4 (not-acceptable) and 3 (marginal), respectively, after 180 d of natural aging. Lastly, it

was notable that, regardless of aging condition, Fe content, and bulk alloy composition, the high cold work variant always yielded an acceptable hem rating (*i.e.*, 2).

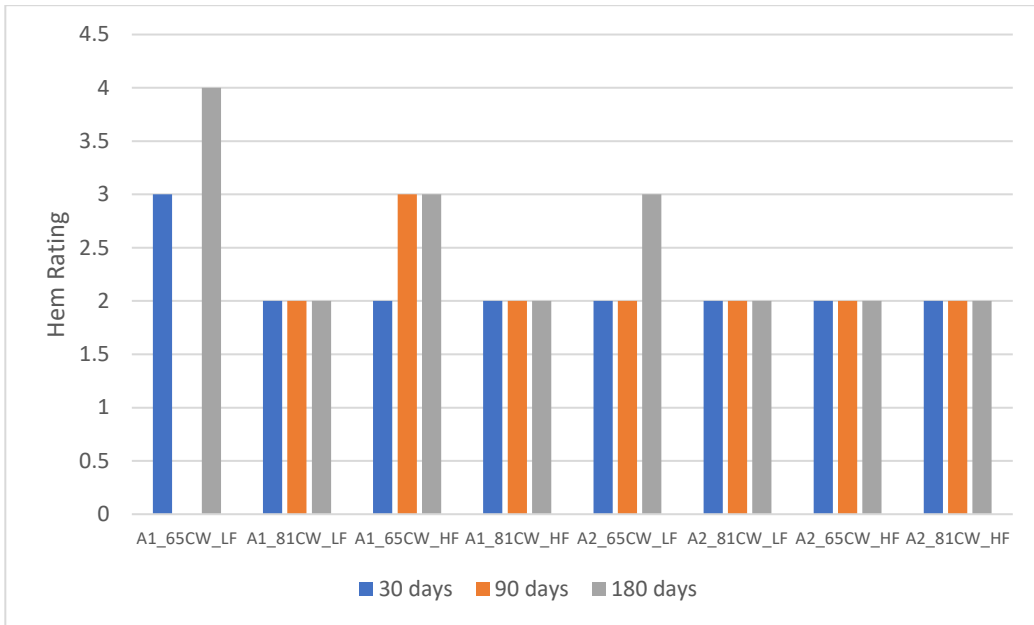


Figure 26: Hem ratings (L direction oriented parallel to the bend line) as a function of natural aging time for each tested alloy condition.

Representative optical images of the hem for each condition after 180 d of natural aging are shown in Figure 25. While these results are consistent with expectations based on the hem ratings shown in Figure 26, the image for A2_65CW_LF underscores the challenge associated with the qualitative ranking scheme for hems. Specifically, examination of 90 d natural aging (Figure 27) reveals the beginning visual signs of cracking, indicating that it was a borderline 2 or 3. The beginning signs of cracking are noted by the red marks in the image of 90 d natural aging. Such an evaluation helps to explain the apparent deviation of this material condition from the general trend of the low cold work alloys and further underscores the improvement in hemmability after more extensive cold work.



Figure 27: Images of A2_65CW_LF flat hems after 30, 90, and 180 d of natural aging.

4.0 Discussion

A summary of the collected microstructural parameters and mechanical properties after 180 d of natural aging, including hem rating, are provided for all tested alloy conditions in Table 6 below. While complete decoupling of the role that interrelated factors have on the formability of Fe-heavy 6xxx-series alloys is non-trivial, the significant dataset presented in Table 6 provides an opportunity to assess the two governing hypotheses posed in Section 1.5:

1. Decreasing the the Si-to-Mg ratio within the required bounds for AA6022 will reduce the effect of increased Fe content on alloy formability
2. Increasing the degree of cold work will reduce the effect of increased Fe content on alloy formability

Table 6: Summary of microstructural and mechanical (after 180 d of natural aging) metrics for each alloy condition; note that TYS is in MPa, VDA is in degrees, and GS is in μm .

Alloy ID	f/r	Bulk/Surface GS	Cube %	After 180 d of Natural Aging				
				n	r	TYS (LT)	VDA (L)	Hem (L)
A1_65CW_LF	0.667	48/105	13	0.240375	0.309	128	115.6	4
A1_81CW_LF	1.837	35/47	22	0.2323	0.233	124	101.5	2
A1_65CW_HF	2.011	41/47	16	0.23725	0.232	121	118.7	3
A1_81CW_HF	1.986	32/36	21	0.23275	0.249	126	107.7	2
A2_65CW_LF	1.576	40/46	11	0.2345	0.278	115	112.2	3
A2_81CW_LF	1.329	34/34	18	0.229	0.242	119	117.2	2
A2_65CW_HF	0.332	36/43	12	0.231625	0.309	116	113.8	2
A2_81CW_HF	1.62	30/33	24	0.228125	0.242	118	117.6	2

In addition to address the two hypotheses, the following discussion will also leverage the data from Table 6 to inform the correlation of mechanical properties with the hem rating that was ultimately

measured for each alloy. Establishing such correlations is industrially useful for informing future materials design activities and performing initial screening of candidate material systems.

4.1 Role of Cold Work and Minor Primary Element Modifications for Creating Fe-Tolerant Automotive Al Sheet Alloys

Increased utilization of aluminum scrap for manufacturing new automotive aluminum sheet is expected to cause the accumulation of trace elements; for example, Fe content increases are anticipated in scrap-based aluminum alloys due to interactions with metal shredding equipment and steel contamination in the scrap recycling stream[10]. According to Banabic, formability is determined by numerous factors, including their capacity of the alloy for strain hardening, the chemical composition, grain morphology and crystallographic texture, and size and distribution of intermetallic particles [56]. Given that Fe is a primary component of common constituent particles in Al alloys, which are known to refine the final grain size and decrease the ductility of 6xxx-series sheet alloys [10, 57, 58], it is likely that these accumulations will modify alloy formability, especially hemming performance. As such, the goal of the current study was to assess whether the influence of increased Fe content (up to the level allowed for trace elements in 6xxx-series alloys; less than 0.15 wt. %) on the hem rating could be mitigated through modifications in either primary alloying element composition or extent of cold work.

Regarding the former, comparison of Alloy 1 to Alloy 2 at similar cold work and Fe content enables the evaluation of Si:Mg ratio (Alloy 1 was ~1.4, while Alloy 2 was ~1.0; Table 2) on hemming performance. Examination of Table 6 above reveals that Alloy 1 exhibited reduced hemming performance (on average; had one 4, one three, and two 2 ratings) as compared to the lower Si:Mg ratio-containing Alloy 2 (three 2s, one 3 rating). Moreover, Table 6 also reveals that Alloy 1 also exhibited increased yield strength and strain hardening exponent (n) for a given extent

of cold work and Fe content. Considering the influence of Si-Mg ratio, both results are consistent with expectations for an increasing Si content. Specifically, numerous studies have demonstrated that increasing the Si content of Al-Mg-Si alloys will generally act to reduce the formability (both from a stretch and bending perspective) and increase the yield strength [59-63]. However, while these effects are noted when Alloy 1 is broadly compared to Alloy 2, the current evidence does not provide clear support for a governing role of bulk alloy composition for attenuating the effect of increasing Fe content. Specifically, the data presented in Table 6 suggests that other contributors play a more important role, as the low Fe-content version of Alloy 1 with 65% cold work was actually the lowest performing material tested (for all evaluated conditions). This result stands in direct contrast to the lowest performing version of Alloy 2, which was the low cold work, high Fe content alloy. As such, while changes in the bulk alloy composition will affect the alloy microstructure (such as Mg_2Si formation) and lead to changes in properties like formability and strength, the current results suggest that other properties/parameters are more important for mitigating the effect of high Fe content on formability.

The observation that the low cold work alloys (Table 6) consistently underperformed the hemming behavior of the high cold work alloys for a given bulk composition and Fe content indicates that cold work could play a key role in mitigating Fe content effects. Literature establishes that increasing the level of cold work generally acts to (1) decrease the average grain size and (2) reduce the average constituent particle size. Examination of Table 6 demonstrates that f/r (which quantifies the Fe-rich particle character) is similar between select low and high Fe content alloys that exhibited different hemming performance. This strongly suggests that the nature of the constituent particle distribution is potentially playing less of an important role than grain size modifications. Note that this interpretation is not suggesting that constituent particle character

does not matter, which would be clearly disputed by literature. Instead, it is proposed that this effect is more secondary in nature, likely through the linkage between f/r and grain size documented in Figure 15 in Section 3 [64]. This postulation is supported by a plot of hem rating versus f/r , shown in Figure 28. Specifically, these data indicate there is a f/r less than 0.75 appear to be detrimental, as would be expected for larger size particles, but that further increases beyond $f/r = 1$ have limited effect.

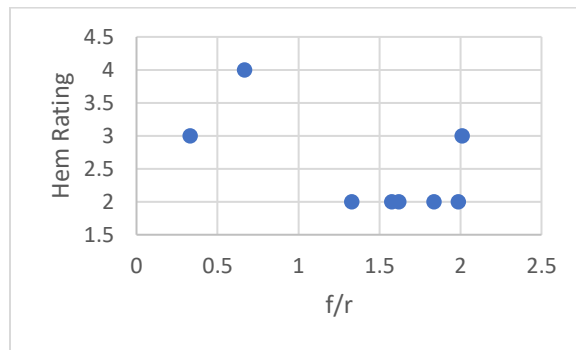


Figure 28: Effect of f/r on hem rating after 180 d of natural aging for each alloy condition.

It therefore follows that the present results instead indicate that grain structure modifications from increased cold work are playing a more causative role. For example, examination of inverse pole figure maps in Figure 14 confirms that the high cold work conditions have both a more uniform and smaller grain size than analogous lower cold work conditions. The positive impact of a smaller grain size is clearly shown in Figure 29 below, which reveals that increasing grain size generally correlates with a higher (and therefore worse) hem rating. Interestingly, the current results (Table 6) also suggest that the formation of a non-uniform grain structure is detrimental to the hemming performance, as demonstrated by poor hem rating of A1_65CW_LF. Such data stands in contrast to isolated literature reports, which have indicated that bimodal grain structures can promote better formability and reduced anisotropy of deformation (i.e., higher r values) [65]. However, it should be noted that this prior study also had

a reference material with distinctly higher grain size than the bimodal alloy, which may have affected the performance comparison.

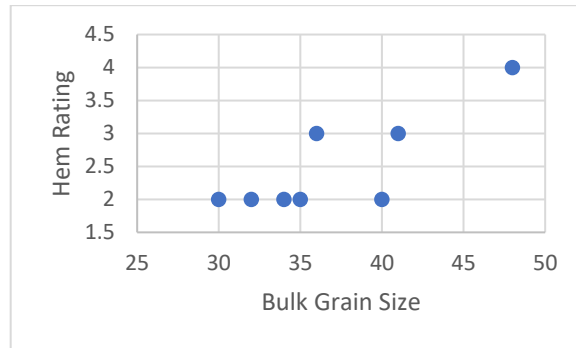


Figure 29: Effect of grain size on the hem rating of each condition after 180 d of natural aging.

In summary, the present results indicate that the increased Fe content can be readily mitigated through the implementation of a higher cold work level. For the evaluated Fe content range, this improvement appears to be induced by the promotion of a more homogeneous and refined grain structure rather than the breaking up of constituent particles. Modifications in bulk alloy composition (specifically Si and Mg ratio) do affect mechanical properties, including formability, but this factor appears to have more global impact irrespective of Fe content. For example, it better correlated with degraded formability and increased yield strength from one bulk composition to another, rather than inducing distinct changes between cold work or Fe content levels within a given alloy).

4.2 Correlation of Bulk Mechanical Properties with Hemming Performance

The specific linkages between alloy processing and hemming performance discussed in the preceding section provide value for understanding approaches to effectively incorporate larger Fe contents into automotive aluminum alloys without sacrificing performance. However, the large dataset generated in this effort also can be leveraged to identify trends between hem rating and other mechanical property measurements. Such insights have long been sought after in the

formability community to help guide alloy down-selection and material design activities. For example, there have been recent efforts to develop formability classification systems for advanced high strength steels that are based on parameters identified from uniaxial tension experiments [66]. For these specific alloys, it has been proposed that the ratio of the true fracture strain and uniform strain can be leveraged to understand whether a given alloy has better local or global formability properties (i.e., bending versus stretching) as well as inform its general overall formability. Other authors have sought to leverage both tensile data and microstructural parameters to inform formability predictions. For example, Antunes and Oliveira proposed a schema based on the strain hardening exponent and stacking fault energy to broadly inform materials selection for hot stamping applications [67].

While the proposed true fracture strain-uniform strain correlations with formability have growing traction in the sheet steels community [68], similar metrics/correlations are not widely reported for aluminum sheet alloys. Literature generally suggests that formability performance for aluminum alloys can be correlated with other metrics, such as n-value and r-value, but discussion of these factors is often in the context of single materials rather than larger datasets. It is therefore useful to leverage the large dataset of mechanical testing and formability measurements to assess the efficacy of specific mechanical properties to serve as a proxy for formability. Towards this end, the hem ratings for all tested conditions in the current study are plotted below in Figure 30 as a function of parameters such as the measured VDA bend angle, n-value, r-value, and r_m after 180 d of natural aging.

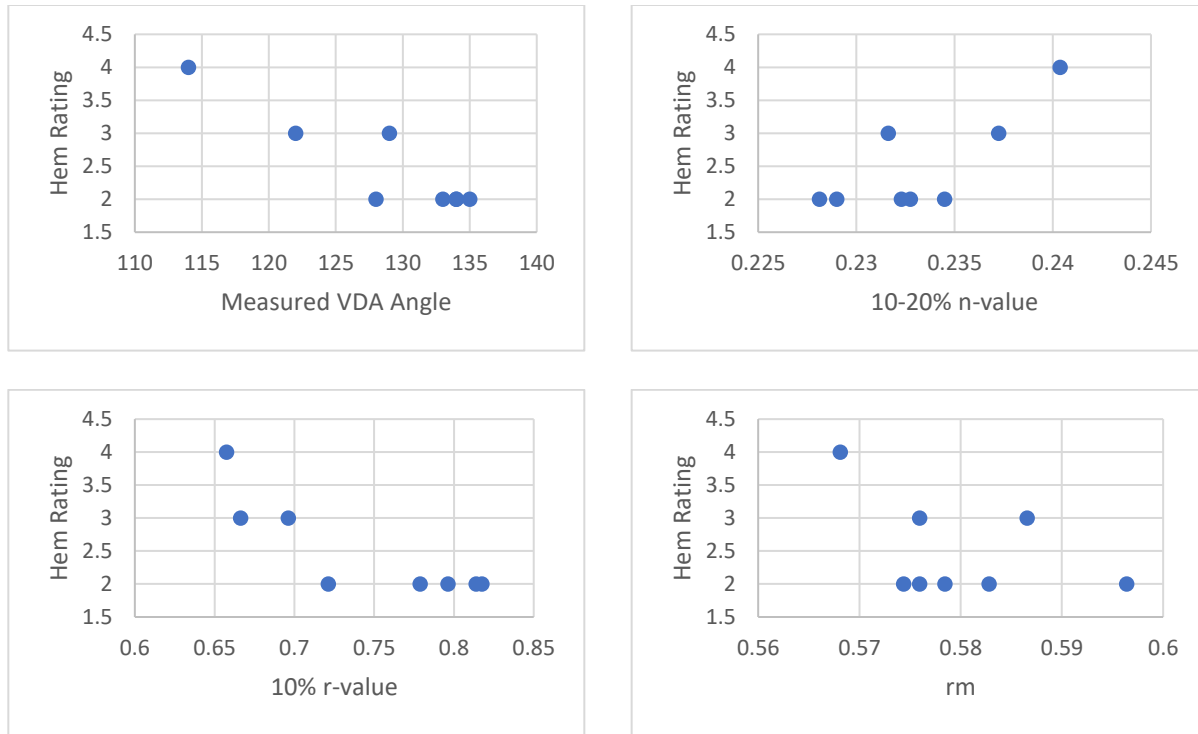


Figure 30: Comparison of mechanical testing metrics and measured hem ratings at 180 d of natural aging

Considering each metric in turn, the current results suggest that there is a strong correlation between hem rating and measured VDA angle, with increasing VDA angle yielding a lower (more favorable) hem rating. Given that this experiment approximately mimics the hem process, such agreement is not unexpected. Interestingly, the results shown in Figure 30 suggest that a VDA angle greater than 130° resulted in a favorable hem performance (rating of 2 or better), suggesting that such a value could be considered for screening purposes in future evaluations. It is possible that an even lower angle could be considered as a cutoff for screening (i.e., 128°), but this evaluation is complicated by the A2_65CW_HF alloy having a hem rating of 3 (which is considered marginal) for a VDA bend angle of 129°.

The plot of the 10-20% n-value and hem rating shows an apparent correlation between the two metrics, with increasing n-value generally leading to an increase (and therefore worse) hem rating. Given that the n-value is known to describe the true strain at the onset of necking, it follows

that this metric should also be a reasonable descriptor of formability. However, two aspects complicate this correlation or limit its utility. First, n -values measured across the entire population of experiments all reside with a relatively small range from 0.228 to 0.241. Though such differences can be identified in stress-strain curves, the sharp variations in performance over a small window would hinder the use of this metric for material design purposes. Instead, it would likely be more useful for ranking one alloy versus another. Second, the ‘mechanistic’ linkage between n -value and the uniform strain should provide insights into general formability, but hemming is a locally concentrated forming mode that may be better described by the true fracture strain (as postulated in research on advanced high strength steel sheets) [66]. Future work should focus on understanding if similar linkages between the true fracture strain and local formability performance exist for aluminum sheet alloys.

Comparison of the Lankford coefficient (or material resistance to thinning) at 10% strain with the measured hem rating at 180 d revealed an initial improvement (decrease) in hem rating as r -value increased. Interesting, the hem rating was stable at 2 for all r -values beyond 0.72, suggesting that a threshold r -value may exist beyond hemming performance is acceptable. Given that a higher r -value indicates a higher resistance to thinning, it is reasonable that this would correlate well with hem rating. Specifically, since large plastic deformations are occurring at the hem, a lower resistance to thinning would lead to material ‘pinching off’ and easier onset of the fracture process. Conversely, when the r -values obtained parallel to the L, LT, and 45° from the L direction are used to calculate the normal anisotropy ratio (r_m), the correlation with hem rating becomes less clear. This inconsistent relationship between r_m and hem rating is not completely unexpected given that r_m describes the material’s ability to be deformed in the plane of the sheet, which is not descriptive of the actual hem forming mode.

5.0 Conclusions

The current study performed a detailed assessment regarding the effect of bulk composition and cold work on the Fe tolerance of an aluminum sheet alloy used for automotive hems. From the collected microstructural parameters, mechanical properties, and formability measurements, the following conclusions could be made:

1. Modification of the bulk composition (specifically, increasing the Si-to-Mg ratio) was found to increase the strength and reduce the formability for a given Fe content and cold work level. However, these modifications were notable from alloy-to-alloy rather than modifying the performance within a given material (*i.e.*, the same nominal rankings with cold work and Fe content were noted within the higher Si-to-Mg alloy).
2. Conversely, increasing the extent of cold work from 65% to 81% consistently improved the formability across all tested Fe contents and bulk alloy compositions. This behavior is likely driven by an improvement in the grain size uniformity as well as a general reduction in grain size with more cold work. A secondary role of constituent particle character also appears likely based on the linkage between increasing f/r and decreasing grain size observed in the tested materials.
3. Correlation of obtained mechanical property metrics from uniaxial tensile testing and simplified bend testing revealed the following general trends with improved hem rating: (1) increasing VDA bend angle, (2) decreasing strain hardening exponent from 10-20% strain, and (3) increasing r -value (Lankford coefficient). Such data could be leveraged to help inform materials screening activities in future studies.

Given the increased interest in leveraging scrap aluminum for fabricating automotive aluminum sheet, the present results are timely in that they identify a pathway by which the expected increase in Fe content inherent to scrap-based alloys can be effectively mitigated. The thesis also adds to the current understanding through the plotted correlations between the various outputs of mechanical testing and the hem rating. While such correlations are broadly leveraged in the steel sheet industry [66] for alloy development, these approaches are uncommon in the aluminum sheet literature. While by no means comprehensive, the current effort provides an initial evaluation in this direction that can be built upon in future work.

6.0 Recommendation and Future Work

Based on the outcomes of the current study, there are several areas that would benefit from additional evaluations. First, results demonstrate that increasing the extent of cold work improved the hemming performance, even when a large Fe content was present in the alloy. However, whether this pathway for improved formability works for mitigating high Fe content effects during other forming operations (such as stamping), where deformation modes are less plane strain, is unclear. Additional studies should be performed to quantify behavior under these other forming processes.

Second, while there was nominal effect of bulk alloy composition on hemming behavior, the primary influence was found to be the extent of cold work, which likely manifested through an effect on grain size. It has also been postulated by Barlat [54] that texture could play an important role, such as S and copper strength; additional studies should be performed looking at the impact of Fe content and thermomechanical processes on texture formation. Such data could then be used to further optimize the employed thermomechanical processing to impart further improvements in formability.

Third, from a bulk composition perspective, the current study only modified by changing the ratio of Si to Mg. However, modification of these elements only result in ‘alloy to alloy’ changes rather than increased differences as a function of Fe content and cold work level. It would be interesting to study the impact of other elements, such as Mn, to determine whether modification of these factors has more effect within a given alloy. For example, Mn could be more effective at pinning the grain size [69, 70], which could increase the ability of a given alloy to tolerate increases in Fe content.

Lastly, the current work underscores the qualitative nature of hem ratings, which can complicate performance assessment and identification of reliable proxies for alloy performance. A need exists to fine tune hem ratings so that more differentiation can be applied between different materials. Continued advances in in-situ characterization may enable a paradigm shift in this arena, but would have to be scalable and low-cost in order to be adopted. Additionally, continued building on the correlations between hem rating and simple mechanical testing metrics reported in the current thesis are needed.

Bibliography

- [1] D. Gohlke, J. Kelly, T. Stephens, X. Wu, Y. Zhou, Mitigation of emissions and energy consumption due to light-duty vehicle size increases, *Transp Res D Transp Environ.* 114 (2023) 103543. <https://doi.org/10.1016/j.trd.2022.103543>.
- [2] C. Kormos, J. Axsen, Z. Long, S. Goldberg, Latent demand for zero-emissions vehicles in Canada (Part 2): Insights from a stated choice experiment, *Transp Res D Transp Environ.* 67 (2019) 685–702. <https://doi.org/10.1016/j.trd.2018.10.010>.
- [3] W.S. Miller, L. Zhuang, J. Bottema, A.J. Wittebrood, P. De Smet, A. Haszler, A. Vieregge, Recent development in aluminium alloys for the automotive industry, *Materials Science and Engineering: A.* 280 (2000) 37–49. [https://doi.org/10.1016/S0921-5093\(99\)00653-X](https://doi.org/10.1016/S0921-5093(99)00653-X).
- [4] F. Czerwinski, Current Trends in Automotive Lightweighting Strategies and Materials, *Materials.* 14 (2021) 6631. <https://doi.org/10.3390/ma14216631>.
- [5] J.M. Luk, H.C. Kim, R. De Kleine, T.J. Wallington, H.L. MacLean, Review of the Fuel Saving, Life Cycle GHG Emission, and Ownership Cost Impacts of Lightweighting Vehicles with Different Powertrains, *Environ Sci Technol.* 51 (2017) 8215–8228.
- [6] Y. Wang, Q. M. (2021). The Impact of the Corporate Average Fuel Economy Standards on Technological Changes in Automobile Fuel Efficiency. *Resource and Energy Economics* <https://doi.org/10.1021/acs.est.7b00909>
- [7] J.C. Kelly, Q. Dai, Life-Cycle Analysis of Vehicle Lightweighting: A Review, in: *Electric, Hybrid, and Fuel Cell Vehicles*, Springer New York, New York, NY, 2021: pp. 91–104. https://doi.org/10.1007/978-1-0716-1492-1_1080.
- [8] Y. Zhu, L.B. Chappuis, R. De Kleine, H.C. Kim, T.J. Wallington, G. Luckey, D.R. Cooper,

- The coming wave of aluminum sheet scrap from vehicle recycling in the United States, *Resour Conserv Recycl.* 164 (2021). <https://doi.org/10.1016/j.resconrec.2020.105208>.
- [9] A. Poznak, D. Freiberg, P. Sanders, Automotive Wrought Aluminium Alloys, in: R.N. Lumley (Ed.), *Fundamentals of Aluminum Metallurgy*, Elsevier, Duxford, UK, 2018: pp. 333–386. <https://doi.org/10.1016/B978-0-08-102063-0.00010-2>.
- [10] D. Raabe, D. Ponge, P.J. Uggowitzer, M. Roscher, M. Paolantonio, C. Liu, H. Antrekowitsch, E. Kozeschnik, D. Seidmann, B. Gault, F. De Geuser, A. Deschamps, C. Hutchinson, C. Liu, Z. Li, P. Prangnell, J. Robson, P. Shanthraj, S. Vakili, C. Sinclair, L. Bourgeois, S. Pogatscher, Making sustainable aluminum by recycling scrap: The science of “dirty” alloys, *Prog Mater Sci.* 128 (2022). <https://doi.org/10.1016/j.pmatsci.2022.100947>.
- [11] A. Bandivadekar, *On the Road in 2035: Reducing Transportation's Petroleum Consumption and GHG Emissions*. Massachusetts Institute of Technology, (2008).
- [12] J. Cui, *Recycling of automotive aluminum*, *Transactions of Nonferrous Metals Society of China*, (2010)
- [13] A. T. Tabereaux, (2014). *Treatise on Process Metallurgy*. Stockholm, Sweden: Elsevier
- [14] W.T. Choate, J.A.S. Green, Modeling the Impact of Secondary Recovery (Recycling) on the U.S. Aluminum Supply and Nominal Energy Requirements, in: Tabereaux. A.T. (Ed.), *Light Metals 2004*, TMS, Warrendale, PA, 2004: pp. 913–918.
- [15] The Aluminum Association. (2021). *Aluminum Sector Snapshot: Environmental Reporting*.
- [16] S.K. Das, J.A.S. Green, J.G. Kaufman, The development of recycle-friendly automotive aluminum alloys, *JOM.* 59 (2007) 47–51. <https://doi.org/10.1007/s11837-007-0140-2>.
- [17] K. Daehn, R. Basuhi, J. Gregory, M. Berlinger, V. Somjit, E.A. Olivetti, Innovations to

- decarbonize materials industries, *Nat Rev Mater.* 7 (2021) 275–294.
<https://doi.org/10.1038/s41578-021-00376-y>.
- [18] M. Mahfoud, D. Emadi, Aluminum Recycling - Challenges and Opportunities, *Adv Mat Res.* 83–86 (2009) 571–578. <https://doi.org/10.4028/www.scientific.net/AMR.83-86.571>
- [19] S.K. Das, Emerging Trends in Aluminum Recycling, in: J.A.S. Green (Ed.), *Aluminum Recycling and Processing for Energy Conservation and Sustainability*, ASM International, 2007: pp. 147–156.
- [20] X. Xu, Z. Liu, B. Zhang, H. Chen, J. Zhang, T. Wang, K. Zhang, J. Zhang, P. Huang, Effect of Mn content on microstructure and properties of 6000 series aluminum alloy, *Applied Physics A.* 125 (2019) 490. <https://doi.org/10.1007/s00339-019-2780-9>.
- [21] Y. Zou, Q. Liu, Z. Jia, Y. Xing, L. Ding, X. Wang, The intergranular corrosion behavior of 6000-series alloys with different Mg/Si and Cu content, *Appl Surf Sci.* 405 (2017) 489–496. <https://doi.org/10.1016/j.apsusc.2017.02.045>.
- [22] T. Wang, X. Xu, J. Zhang, H. Chen, C. Zhu, J. Zhang, K. Zhang, Effect of Mg on microstructure and properties of 6000 series high strength and high ductility aluminum alloy, *Mater Res Express.* 6 (2019) 0865a7. <https://doi.org/10.1088/2053-1591/ab214d>.
- [23] G.H. Tao, C.H. Liu, J.H. Chen, Y.X. Lai, P.P. Ma, L.M. Liu, The influence of Mg/Si ratio on the negative natural aging effect in Al–Mg–Si–Cu alloys, *Materials Science and Engineering: A.* 642 (2015) 241–248. <https://doi.org/10.1016/j.msea.2015.06.090>.

- [24] G. Svenningsen, J.E. Lein, A. Bjørgum, J.H. Nordlien, Y. Yu, K. Nisancioglu, Effect of low copper content and heat treatment on intergranular corrosion of model AlMgSi alloys, *Corros Sci.* 48 (2006) 226–242. <https://doi.org/10.1016/j.corsci.2004.11.025>.
- [25] M.H. Larsen, J.C. Walmsley, O. Lunder, K. Nisancioglu, Effect of Excess Silicon and Small Copper Content on Intergranular Corrosion of 6000-Series Aluminum Alloys, *J Electrochem Soc.* 157 (2010) C61. <https://doi.org/10.1149/1.3261804>.
- [26] A. Jaafar, A. Rahmat, Z. Hussain, I. Zainol, Effect of Mg, Si and Cu content on the microstructure of dilute 6000 series aluminium alloys, *J Alloys Compd.* 509 (2011) 8632–8640. <https://doi.org/10.1016/j.jallcom.2011.05.061>.
- [27] S.M. Hirth, G.J. Marshall, S.A. Court, D.J. Lloyd, Effects of Si on the aging behaviour and formability of aluminium alloys based on AA6016, *Materials Science and Engineering: A.* 319–321 (2001) 452–456. [https://doi.org/10.1016/S0921-5093\(01\)00969-8](https://doi.org/10.1016/S0921-5093(01)00969-8).
- [28] S. Esmaeili, D.J. Lloyd, The Role of Copper in the Precipitation Kinetics of 6000 Series Al Alloys, *Materials Science Forum.* 519–521 (2006) 169–176. <https://doi.org/10.4028/www.scientific.net/MSF.519-521.169>.
- [29] Z. Li, Z. Zhang, G. Zhou, P. Zhao, Z. Jia, W.J. Poole, The effect of Mg and Si content on the microstructure, texture and bendability of Al–Mg–Si alloys, *Materials Science and Engineering: A.* 814 (2021) 141199. <https://doi.org/10.1016/j.msea.2021.141199>.

- [30] M.S. Remøe, K. Marthinsen, I. Westermann, K. Pedersen, J. Røyset, C. Marioara, The effect of alloying elements on the ductility of Al-Mg-Si alloys, *Materials Science and Engineering: A*. 693 (2017) 60–72. <https://doi.org/10.1016/j.msea.2017.03.078>.
- [31] J.B. Hess, Physical metallurgy of recycling wrought aluminum alloys, *Metallurgical Transactions A*. 14 (1983) 323–327. <https://doi.org/10.1007/BF02644210>.
- [32] S. Zhu, J.-Y. Yao, L. Sweet, M. Easton, J. Taylor, P. Robinson, N. Parson, Influences of Nickel and Vanadium Impurities on Microstructure of Aluminum Alloys, *JOM*. 65 (2013) 584–592. <https://doi.org/10.1007/s11837-013-0572-9>.
- [33] S. Camero, E.S. Puchi, G. Gonzalez, Effect of 0.1% vanadium addition on precipitation behavior and mechanical properties of Al-6063 commercial alloy, *J Mater Sci*. 41 (2006) 7361–7373. <https://doi.org/10.1007/s10853-006-0794-0>.
- [34] J. Grandfield, L. Sweet, C. Davidson, J. Mitchell, A. Beer, S. Zhu, X. Chen, M. Easton, An Initial Assessment of the Effects of Increased Ni and V Content in A356 and AA6063 Alloys, in: 2016: pp. 39–45. https://doi.org/10.1007/978-3-319-65136-1_7.
- [35] Sarkar, J., Kutty, T. R. G., Wilkinson, D. S., Embury, J. D., & Lloyd, D. J. (2004). Tensile properties and bendability of T4 treated AA6111 aluminum alloys. *Materials Science and Engineering: A*, 369(1-2), 258-266.
- [36] Y. Meng, J. Cui, Z. Zhao, Y. Zuo, Effect of vanadium on the microstructures and

- mechanical properties of an Al–Mg–Si–Cu–Cr–Ti alloy of 6XXX series, *J Alloys Compd.* 573 (2013) 102–111. <https://doi.org/10.1016/j.jallcom.2013.03.239>.
- 37] B. Trink, I. Weißensteiner, P. J. Uggowitzer, K. Strobel, S. Pogatscher, High Fe content in Al-Mg-Si wrought alloys facilitates excellent mechanical properties, *Scripta Materialia* 215 (2022). <https://doi.org/10.1016/j.scriptamat.2022.114701>.
- 38] Y. Tang, Y. Tomita, Z. Horita, Mechanical Properties and Microstructures of Highly Fe-Containing Al–Mg–Si Alloys Processed by Severe Plastic Deformation under High Pressure, *Materials Transactions.* 64 (2023) 102–111. <https://doi.org/10.1016/j.jallcom.2013.03.239>.
- 39] S. Murtha, New 6XXX Aluminum Alloy for Automotive Body Sheet Applications, *SAE Transactions*, (1995)
- 40] P. E. Jimbert, Straight Hemming of Aluminum Sheet Panels Using Electromagnetic Forming Technology: First Approach, *Key Engineering Materials*, (2007)
- [41] H. S. Lui, Pre-Aging and Microstructures Properties on 6000 Series Aluminium Alloys for Automotive Body Sheets. *Chinese Journal of Nonferrous Metals* (2005).
- [42] *E1251-17 Standard Test Method for Analysis of Aluminum and Aluminum Alloys by Spark Atomic Emission Spectrometry*, West Conshohocken: ASTM International, (2021).
- [43] J. E. Hatch, *Aluminum: Properties and Physical Metallurgy*. Metals Park: American Society for Metals, (1998).
- [44] *E1251-17 Standard Guide for Preparation of Metallographic Specimens*, West Conshohocken: ASTM International, (2017).
- [45] G. VanderVoort, *ASM Handbook Volume 9: Metallography and Microstructures*. Metals Park: American Society for Metals (2004).

- [46] E2627-13 Standard Practice for Determining Average Grain Size Using Electron Backscatter Diffraction (EBSD) in Fully Recrystallized Polycrystalline Materials. West Conshohocken: ASTM International. (2019).
- [47] E112-13 Standard Test Methods for Determining Average Grain Size. West Conshohocken: ASTM International (2021).
- [48] E8 Standard Test Methods for Tension Testing of Metallic Materials, West Conshohocken: ASTM International, (2022).
- [49] Komvopoulos, K. *Mechanical Testing of Engineering Materials*. San Diego: Cognella Academic Publishing, (2017).
- [50] G. E. Dieter, *Mechanical Metallurgy*. London: McGraw-Hill, 3rd Ed, (1988)
- [51] Cheong, K. (2017). Evaluation of the VDA 238-100 Tight Radius Bending Test using Digital Image Correlation Strain Measurement. *Journal of Physics*.
- [52] Verband der Automobilindustrie. (2017). *Plate bending test for metallic materials*. Berlin.
- [53] G. E. Totten, *Handbook of Aluminum*. Milton Park: Taylor and Francis,(2003).
- [54] F. Barlat, Crystallographic Texture, Anisotropic Yield Surfaces and Forming Limit of Sheet Metals. *Materials Science and Engineering*, (1987).
- [55] H Lu, J. Zhang, N. Tian, X. Song, M. Ma, G. Lu, Recycle-Friendly Aluminum Alloy Sheets for Automotive Applications Based on Hemming. *Automotive Innovation* (2018). 1. 10.1007/s42154-018-0012-1.
- [56] D. Banabic, *Sheet Metal Forming Processes: Constitutive Modelling and Numerical Simulation*. New York: Springer, (2010).
- [57] H. Lu, J. Zhang, N. Tian, X. Song, M. Ma, G. Lu, Recycle-Friendly Aluminum Alloy Sheets for Automotive Applications Based on Hemming, *Automotive Innovation*. 1 (2018) 70–

75. <https://doi.org/10.1007/s42154-018-0012-1>.
- [58] J. Sarkar, T. R. G. Kutty, D. S. Wilkinson, J. D. Embury, J. D., & Lloyd, D. J. Tensile properties and bendability of T4 treated AA6111 aluminum alloys. *Materials Science and Engineering: A*, 369(1-2), 258-266. (2004).
- [59]] H. Zhong, P. A. Rometsch, L. Cao, Estrin, Y, The influence of Mg/Si ratio and Cu content on the stretch formability of 6xxx aluminium alloys. *Materials Science and Engineering A*, 651, 688–697, (2016).
- [60] S. M. Hirth, G. J. Marshall, S. A. Court, D. J. Lloyd, (2001). Effects of Si on the aging behaviour and formability of aluminium alloys based on AA6016. In *Materials Science and Engineering* (2001).
- [61] P. Zhao, Z. Jia, W. J. Poole, The effect of Mg and Si content on the microstructure, texture and bendability of Al–Mg–Si alloys, *Materials Science and Engineering* (2021).
- [62] A. Thum, A. Shafiee Sabet, N. Müllner, W. Fragner, C. Sommitsch, Influence of alloy composition and lubrication on the formability of Al-Mg-Si alloy blanks, *Journal of Manufacturing Processes* (2023). 109–121.
<https://doi.org/10.1016/j.jmapro.2022.11.029>
- [63] R. E. Sanders, Q. Liu, G. Yang, The natural aging and precipitation hardening behaviour of Al-Mg-Si-Cu alloys with different Mg/Si ratios and Cu additions, *Materials Science and Engineering* (2015)
- [64] P. A. Manohar, Five Decades of the Zener Equation. *ISIJ International*, Vol. 38 (1998).
- [65] M.X. Guo, J. Zhu, Y. Zhang, G.J. Li, T. Lin, J.S. Zhang, L.Z. Zhuang, The formation of bimodal grain size distribution in Al-Mg-Si-Cu alloy and its effect on the formability, *Materials Characterization* 132 (2017)

[66] Hance, B. M. "Advanced high strength steel: Deciphering local and global formability." Proc. International Automotive Body Congress, Dearborn, MI. Vol. 2. 2016.

[67] Antunes, Renato Altobelli, and Mara Cristina Lopes de Oliveira. "Materials selection for hot stamped automotive body parts: An application of the Ashby approach based on the strain hardening exponent and stacking fault energy of materials." *Materials & Design* 63 (2014): 247-256.

[68] Pelligra, C., Samei, J., Kang, J., & Wilkinson, D. S. (2022). The effect of vanadium on microstrain partitioning and localized damage during deformation of unnotched and notched DP1300 steels. *International Journal of Plasticity*, 158, 103435.

[69] F. C. Campbell, *Elements of Metallurgy and Engineering Alloys*. Metals Park, OH: American Society for Metals, (2008).

[70] J. R. Davis, J. R., *Aluminum and Aluminum Alloys*. Metals Park, OH: American Society for Metals, (1993).